Monthly Notices
of the
ROYAL ASTRONOMICAL SOCIETY

MNRAS **439,** 3094–3113 (2014)
Advance Access publication 2014 February 20

doi:10.1093/mnras/stu172

Precision radial velocities of 15 M5–M9 dwarfs

J. R. Barnes,[1]★ J. S. Jenkins,[2] H. R. A. Jones,[1] S. V. Jeffers,[3] P. Rojo,[2] P. Arriagada,[4] A. Jordán,[4] D. Minniti,[4,5] M. Tuomi,[1,6] D. Pinfield[1] and G. Anglada-Escudé[7]

[1]*Centre for Astrophysics Research, University of Hertfordshire, College Lane, Hatfield, Hertfordshire AL10 9AB, UK*
[2]*Departamento de Astronomía, Universidad de Chile, Camino del Observatorio 1515, Las Condes, Santiago, Chile*
[3]*Institut für Astrophysik, Georg-August-Universität, Friedrich-Hund-Platz 1, Friedrich-Hund-Platz 1, D-37077 Göttingen, Germany*
[4]*Instituto de Astrofísica, Pontificia Universidad Católica de Chile, Av. Vicuña Mackenna 4860, 7820436 Macul, Santiago, Chile*
[5]*Vatican Observatory, I-V00120 Vatican City State, Italy*
[6]*University of Turku, Tuorla Observatory, Department of Physics and Astronomy, Väisäläntie 20, FI-21500 Piikkiö, Finland*
[7]*Astronomy Unit, School of Physics and Astronomy, Queen Mary, University of London, Mile End Road, London E1 4NS, UK*

Accepted 2014 January 21. Received 2014 January 21; in original form 2013 October 26

ABSTRACT

We present radial velocity measurements of a sample of M5V–M9V stars from our Red-Optical Planet Survey, operating at 0.652–1.025 μm. Radial velocities for 15 stars, with rms precision down to 2.5 m s^{-1} over a week-long time-scale, are achieved using thorium–argon reference spectra. We are sensitive to planets with $m_{\rm p} \sin i \geq 1.5\,{\rm M}_{\oplus}$ ($3\,{\rm M}_{\oplus}$ at 2σ) in the classical habitable zone, and our observations currently rule out planets with $m_{\rm p} \sin i > 0.5\,M_{\rm J}$ at 0.03 au for all our targets. A total of 9 of the 15 targets exhibit rms < 16 m s^{-1}, which enables us to rule out the presence of planets with $m_{\rm p} \sin i > 10\,{\rm M}_{\oplus}$ in 0.03 au orbits. Since the mean rotation velocity is of the order of 8 km s^{-1} for an M6V star and 15 km s^{-1} for M9V, we avoid observing only slow rotators that would introduce a bias towards low axial inclination ($i \ll 90^{\circ}$) systems, which are unfavourable for planet detection. Our targets with the highest $v \sin i$ values exhibit radial velocities significantly above the photon-noise-limited precision, even after accounting for $v \sin i$. We have therefore monitored stellar activity via chromospheric emission from the Hα and Ca II infrared triplet lines. A clear trend of $\log_{10}(L_{\rm H\alpha}/L_{\rm bol})$ with radial velocity rms is seen, implying that significant starspot activity is responsible for the observed radial velocity precision floor. The implication that most late M dwarfs are significantly spotted, and hence exhibit time varying line distortions, indicates that observations to detect orbiting planets need strategies to reliably mitigate against the effects of activity-induced radial velocity variations.

Key words: techniques: radial velocities – planets and satellites: detection – stars: activity – stars: atmospheres – stars: low-mass – planetary systems.

1 INTRODUCTION

Although the solar neighbourhood is dominated by low-mass stars, the late M dwarf population has remained largely beyond the reach of optical precision radial velocity (RV) surveys. In order to address this major parameter space, dedicated instruments have been proposed that would instead operate at longer wavelengths, at the peak of the energy distribution of low-mass stars (Jones et al. 2008). Upcoming instruments are now being constructed, and include the Habitable Zone Planet Finder (Mahadevan et al. 2012) and CARMENES, the Calar Alto high-Resolution search for M dwarfs with Exo-earths with Near-infrared and optical Echelle Spectrometers (Quirrenbach et al. 2012). However, while a number of well-established instruments with proven stability at earlier spectral types have also reported precision RVs for early M dwarfs, the CRyogenic high resolution InfraRed Échelle Spectrometer (CRIRES) survey (Bean et al. 2010) and the Red-Optical Planet Surve (ROPS; Barnes et al. 2012, hereafter B12) have reported precision RVs at the ∼10 m s^{-1} level for late M dwarfs (M6V–M9V) with existing instrumentation. Reiners (2009) has also reported ∼10 m s^{-1} stability on the flaring M6 dwarf CN Leo. Working in the infrared *K* band, Bean et al. (2010) reported 11.7 m s^{-1} for Proxima Cen, and 5.4 m s^{-1} after observations were binned together. On the other hand, B12, working in the red-optical (0.62–0.90 μm), found that while propagated errors were at the ∼10 m s^{-1} level, the rms scatter was 16–35 m s^{-1} in the most stable targets. Until CRIRES is upgraded to a cross-dispersed, multi-order instrument, Ultraviolet and Visual Echelle Spectrograph (UVES) has substantially more wavelength coverage with reasonable signal-to-noise (S/N) from

★ E-mail: j.r.barnes@herts.ac.uk

which RVs may be derived. UVES has also already demonstrated 2–2.5 m s^{-1} precision over 7 yr working with an I_2 cell (Zechmeister, Kürster & Endl 2009) in the 5000–6000 Å range. However, by ∼6500 Å, I_2 lines become weak (<10 per cent of the normalized continuum) and are barely visible beyond 7000 Å. Hence, I_2 gas cells cannot be used in the red part of the optical, beyond these wavelengths.

The first planet orbiting an M dwarf was reported by Delfosse et al. (1998) and Marcy et al. (1998) nearly a decade after the first low-mass companion to the main-sequence star HD 114762 (Latham et al. 1989), which may be either a brown dwarf or massive planet, depending on the unknown orbital inclination. GJ 876 b, orbiting its parent M4V star in a 61 d orbit is a giant planet, which is perhaps not surprising given that close-orbiting companions are the easiest to detect with few epochs of observations using RV techniques. However, while close-orbiting planets have been predicted to be relatively common for early M dwarf samples (see Section 1.1 below), only ∼50 per cent of the M dwarf planets with mass estimates (16 from a total of 31)[1] possess masses $\gtrsim$0.3 M_J. The remaining 15 planets have minimum masses implying Super-Earth to Neptune-mass companions. GJ 876 b is only one of four planets so far detected orbiting GJ 876, and in fact two of the planets possess masses of only 5.8 and 12.5 $M_\oplus$. In addition, amongst the Kepler candidates first reported by Borucki et al. (2011) and confirmed by a number of authors (Fabrycky et al. 2012; Muirhead et al. 2012; Steffen et al. 2013), 14 planets have been identified with radii $\leq$3 $R_\oplus$, whilst no transiting hot Jupiters have been detected. To date these findings confirm earlier predictions that Neptune-mass and Earth-mass planets are expected in greater numbers in orbit around M stars (Ida & Lin 2005).

1.1 Rocky planet occurrence rates and the M dwarf habitable zone

Bonfils et al. (2013) have calculated phase-averaged detection limits for individual stars, which enable the survey efficiency of the HARPS (High Accuracy Radial velocity Planet Searcher) early M dwarf sample to be determined. These detection limits enable corrections to be made for incompleteness, allowing occurrence rates to be estimated. The frequency of HZ planets, $\eta_\oplus$ (where $1 < m \sin i < 10\,M_\oplus$), orbiting early M dwarfs is found to be $0.36^{+0.25}_{-0.10}$. From the Kepler sample, Dressing & Charbonneau (2013) estimated $\eta_\oplus = 0.90^{+0.04}_{-0.03}$ for M dwarf planets up to 4 $R_\oplus$. With revised estimates of habitable zones (HZ; Kopparapu et al. 2013), Kopparapu (2013) used the 95 Kepler planet candidates orbiting 64 low-mass host stars to similarly place conservative estimates of $\eta_\oplus = 0.51^{+0.10}_{-0.20}$ for M dwarf planets with radii in the range 0.5–2 $R_\oplus$. Bonfils et al. (2013) find that the majority of *early* M dwarf planets are clustered in few-day to tens of days orbits, continuing the trend with semi-major axis distribution observed by Currie (2009). By extrapolation, we might expect *late* M dwarf planets in orbits up to a few tens of days.

The centre of the continuous HZ for an M6V star is estimated to be ∼0.045 au (Kopparapu et al. 2013). Hence, a 7.5 $M_\oplus$ planet would induce a $K_* = 10$ m s^{-1} signal with an 11.0 d period. Although Kopparapu et al. (2013) do not make HZ estimates for low masses, based on a simple flux and mass scaling, we estimate that an M9V star HZ would be centred at ∼0.023 au, with a 7.5 $M_\oplus$ planet inducing a 15.8 m s^{-1} signal with a 4.4 d period. Observations spanning a 6 d period (which we present in this paper) thus offer the potential to sample 55 per cent of an M6V HZ period, and greater than a complete orbit for an M9V star. By defining a continuous HZ, the range of possible orbital periods for habitable planets are extended. For instance, Kopparapu et al. (2013) define inner moist greenhouse and outer greenhouse limits, which extend the range of periods for an M6V habitable planet from ∼6 d to a maximum of ∼17 d.

1.2 ROPS sample

Our choice of targets was based on a number of factors including visibility and brightness. In order to obtain sufficient S/N in the spectra in exposures limited to no more than 1800 s, we limited the selection to M5–M9 dwarfs with apparent I-band magnitudes $\lesssim$14.5. A number of stars in common with our initial observations made with the Magellan Inamori Kyocera Échelle (MIKE) spectrograph at Magellan Clay (B12) have been retained. Additional targets were selected, ensuring that a range of spectral types were included with low-moderate $v \sin i$ values. Because M stars, and particularly late M stars on the whole, are not effectively spun down, those stars later than M6V tend to be moderate rotators on the whole. Jenkins et al. (2009) found that M6V stars on average possess $v \sin i$ ∼8 km s^{-1}, whereas this rises to ∼15 km s^{-1} for M9V. This obviously has important consequences for RV precision, especially if magnetic activity phenomena affect the rotation profiles. Because moderate rotation is found on average, selecting only the slowest rotating stars with $v \sin i \leq 5$ km s^{-1} is likely to bias a target sample to low axial inclination ($i \ll 90°$) systems (i.e. with rotation axis aligned along the line of sight to the observer), for which detection of planets is less favourable. In order to characterize the effects of activity for this and future surveys, we included moderate rotators in our sample. The objects were selected for which $v \sin i$ was on the whole well measured (Mohanty & Basri 2003; Reiners & Basri 2010). In addition, following the procedures detailed in Jenkins et al. (2009), we have also obtained the first $v \sin i$ measurements for two of the targets in our sample, GJ 3076 and GJ 3146, as indicated in Table 1.

In this paper, we investigate the methods by which precision RVs can be achieved with existing instrumentation, extending the search of optical spectrometers into the 0.65–1.025 μm wavelength region, where no established simultaneous reference fiducial has been tested. In Section 3, we outline our master wavelength calibration procedure. The use of tellurics for wavelength calibration is investigated in Section 4 using an analysis similar to that carried out by Figueira et al. (2010) for HARPS observations of G-type stars. We derive RVs for Proxima Centauri using only telluric lines to enable us to determine the simultaneous wavelength solution. In Section 5, we present the RV measurement procedures for our ROPS sample, discussing our wavelength calibration procedure (Section 5.2), applicable particularly to UVES observations, before presenting RVs for our 15 M5V–M9V targets from four epochs of observations spread over a week-long time-scale (Section 5.3). Finally, we discuss our findings (Section 5.4) and prospects for future observations (Section 6).

2 OBSERVATIONS

In this paper, we utilize observations made during our own observing campaign in 2012 July. We also use data taken from the European Southern Observatory (ESO) archive.

[1] http://exoplanets.org

Table 1. List of targets observed with UVES with estimated spectral types, *I*-band magnitudes, exposure times and $v \sin i$ values (columns 1 to 5). The measured $v \sin i$ values are taken from Mohanty & Basri (2003), Jenkins et al. (2009) and Reiners & Basri (2010). We derived $v \sin i$'s for GJ 3076 and GJ 3146 (denoted by *) using the procedures we adopted in Jenkins et al. (2009). We also list details for Proxima Centauri and the mean rms of 5.2 m s^{-1}, after atmospheric correction for all three nights, is given. The exposure times† for Proxima Centauri were variable, ranging between 11 and 500 s; however, 74 per cent of the observations were made with 100 s exposures. Extracted S/N ratio and S/N ratio after deconvolution are tabulated in columns 6 and 7. Column 8 lists the total number of observations, N_{obs} on each target and column 9 gives the rms scatter using an $N_{obs} - 1$ correction to account for the small number of observations for each object (see Section 5.3). In columns 10, 11 and 12, we list rms values after applying bisector corrections derived from the stellar line (L), telluric line (T), and both lines (L-T). Discussion of the results is given in Section 5.3.

Star	SpT	Imag	Exp (s)	$v \sin i$ (km s^{-1})	S/N Extracted	Mean S/N Decon	N_{obs}	rms (m s^{-1}) No corr	rms (m s^{-1}) L corr	rms (m s^{-1}) T corr	rms (m s^{-1}) L-T corr
GJ 3076	M5V	10.9	400	17.1*	77 ± 10	6120	4	100.7	92.3	67.6	44.5
GJ 1002	M5.5V	10.2	300	≤3	106 ± 12	9110	4	29.4	5.1	12.9	23.6
GJ 1061	M5.5V	9.5	300	≤5	142 ± 12	12 150	5	4.23	2.4	2.4	2.8
LP 759-25	M5.5V	13.7	1500	13	38 ± 5	2810	4	106.8	79.9	70.6	65.9
GJ 3146	M5.5V	11.3	600	12.4*	60 ± 10	4920	4	87.2	47.1	80.2	7.75
GJ 3128	M6V	11.1	350	≤5	65 ± 3	5590	4	24.4	11.5	24.1	15.6
Proxima Centauri	M6V	6.9	100†	2	191 ± 22	12 900	561	5.2	–	–	–
GJ 4281	M6.5V	12.7	1200	7	49 ± 6	4240	4	36.7	11.7	12.0	15.3
SO J025300.5+165258	M7V	10.7	350	≤5	95 ± 12	8280	4	15.2	12.4	12.5	14.6
LP 888-18	M7.5V	13.7	1500	≤3	36 ± 3	2790	4	45.3	35.3	31.6	38.0
LHS 132	M8V	13.8	500	≤5	37 ± 2	3160	4	12.3	12.3	7.7	9.09
2MASS J23062928−0502285	M8V	14.0	1500	6	38 ± 1	2890	4	29.0	14.2	16.9	10.0
LHS 1367	M8V	13.9	1500	≤5	32 ± 3	2470	4	22.7	15.3	16.1	22.5
LP 412-31	M8V	14	1200	12	26 ± 7	1850	3	253.2	222.6	248.9	119.6
2MASS J23312174−2749500	M8.5V	14.0	1500	6	37 ± 2	2890	4	37.2	36.7	29.5	22.3
2MASS J03341218−4953322	M9V	14.1	1500	8	33 ± 2	2810	4	11.2	6.37	6.92	8.37

2.1 ROPS observations with UVES

We observed 15 m dwarf targets with the UVES at the 8.2 m Very Large Telescope (VLT, UT2). Observations were made with a 0.8 arcsec slit, which give a resolution of $R \sim 54\,000$. We observed on four half nights spread over a period of six nights in total, on 2012 July 23, 24, 26 and 29 (UTC). Short orbital periods might be expected by extrapolating the tens of days orbits, found amongst *early* M dwarfs (Bonfils et al. 2013), to the late M dwarf population. Additionally, the observing strategy enabled the stability of UVES and our measurement precision to be characterized on week-long time-scales. Although UVES offers the ability to simultaneously record observations at shorter and longer wavelengths, we opted to make observations in the red arm only since mid-to-late M stars output little flux short of 6000 Å. In B12, we found the ratio of flux in the 7000–9000 Å region compared with the 5000–7000 Å region to be 11.5 and 19 for M5.5V and M9V spectra, respectively. This estimate included the throughput of the 6.5 m Magellan Clay and MIKE spectrograph.

Working in the red-optical (i.e. 0.6–1.0 μm) poses a particular challenge in that there are no currently operating échelle spectrometers coupled with 8 m class telescopes that offer simultaneous calibration. Regular wavelength observations for calibration are crucial if precisions of the order of m s^{-1} are to be achieved from high-resolution RV information. Although UVES possesses an iodine cell, the absorption lines of I_2 do not extend far above 6500 Å, and are already very weak, with line depths of only a few per cent of the normalized continuum. We have therefore opted to utilize near-simultaneous observations of thorium–argon (ThAr) arc lamp lines, coupled with the relative stability of UVES in order to achieve sub-m s^{-1} precision on our target population of late M stars. Since ThAr lamps exhibit many lines for calibration, and are generally always available by default with échelle spectrometers working at optical wavelengths, we made regular observations with the comparison lamp available with UVES. A calibration was included in the observing block associated with each observed target and was taken immediately after each science frame. Further details on the calibration procedures are given in Section 3 and following sections. The observing conditions over the four half nights were very good, with seeing estimates in the range 0.7–1.2 for targets observed at airmasses <1.5. Our targets are listed in Table 1.

2.2 Proxima Centauri observations

Proxima Centauri has been shown by Endl & Kürster (2008) to be stable to 3.11 m s^{-1} over a 7 yr period and thus we consider this to be a good target to pursue as a calibrator for our techniques. Data taken with UVES, spanning five nights, with observations made on three nights and single night gaps, were obtained from the ESO data archive. These data were initially taken as part of a multiwavelength survey of Proxima Centauri (GJ 551) and are presented in Fuhrmeister et al. (2011). Approximately 560 spectra of Proxima Centauri were continuously recorded on each of the three nights on 2009 March 10, 12 and 14, spanning 8 h per night with altitudes corresponding to an airmass range of 2.41–1.27. A slit width of 1 arcsec gives a spectral resolution, $R \gtrsim 43\,000$, in the red arm of UVES, while the extreme airmass range of the observations led to seeing that varied from 1.4 arcsec at high airmass, down to ∼0.6 arcsec at low airmass. The CCD readout was binned in the wavelength direction by a factor of 2, resulting in an average pixel increment of 2.4 km s^{-1}. The rotation velocity of Proxima Centauri, at $v \sin i = 2$ km s^{-1}, means that spectral resolution (equivalent to ∼6 km s^{-1}) dominates the line width.

2.3 Data extraction

The data sets for both our ROPS sample (Section 2.1) and Proxima Centauri (Section 2.2) were flat-field corrected by using combined

exposures taken with an internal tungsten reference lamp. Since few counts are recorded in the reddest orders of the Massachusetts Institute of Technology Lincoln Laboratory (MITLL) CCD (owing to the spectrograph efficiency and low quantum efficiency of the CCD longwards of 1.0 μm), where of the order of 10 000 counts could be achieved with 14 s exposures compared with a peak of 40 000 counts, an additional 30 flat-field frames were taken in addition to the standard calibrations for the ROPS (Section 2.1) data set. The worst cosmic ray events were removed at the pre-extraction stage using the Starlink FIGARO (Shortridge 1993) routine *bclean* (the Starlink software is currently distributed by the Joint Astronomy Centre[2]). The spectra were extracted using ECHOMOP's implementation of the optimal extraction algorithm developed by Horne (1986). ECHOMOP rejects all but the strongest sky lines (Barnes et al. 2007) and propagates error information based on photon statistics and readout noise throughout the extraction process.

3 WAVELENGTH CALIBRATION

Wavelength calibration at the $m\,s^{-1}$ level is required if precision RVs are to be achieved. To this end, a great deal of effort has been expended in order to obtain accurate wavelengths for spectral calibration references (e.g. Gerstenkorn & Luc 1978). Despite recent work that has identified new sources for calibration, suitable reference lines are often limited in the wavelength regions that they span. Mahadevan & Ge (2009) have identified a number of molecular gas cells that could be used to span the *H* band, while LASER comb technology has also been used to demonstrate $\sim$10 $m\,s^{-1}$ precision on sky in the *H* band (Ycas et al. 2012). Although new calibration sources, rich in lines, have also been identified in the red part of the optical (Redman et al. 2011), ThAr still remains the most regularly used and only available calibration source for optical and infrared high-resolution spectrometers, although with relatively few lines in the near-infrared (>1 μm).

3.1 Master wavelength calibration

ThAr wavelengths published by Lovis & Pepe (2007) were used to identify stable lines for wavelength calibration. This line list is estimated to enable a calibration (i.e. global) rms to better than 20 $cm\,s^{-1}$ for HARPS. Pixel positions were initially identified for a single arc using a simple Gaussian fit. For each subsequent arc, a cross-match was made, followed by a multiple-Gaussian (up to three profiles) fit around each identified line using a Levenberg–Marquardt fitting algorithm (Press et al. 1986) to obtain the pixel position of each line centre. The Lovis & Pepe line list was optimized for HARPS at $R = 110\,000$, while our observations were made at $R \sim 50\,000$ necessitating rejection of some lines that showed blending. Using a multiple-Gaussian fit enables the effect of any nearby lines to be accounted for in the fit that also included a first-order (straight line) background. Any lines closer than the instrumental full width at half-maximum (FWHM) were not used. Finally for each order, any remaining outliers were removed after fitting a cubic polynomial. In addition, any lines that were not consistently yielding a good fit for all arc frames throughout both nights (to within 3σ of the cubic fits) were removed.

The ThAr observation following each star on the second night was chosen arbitrarily as the reference solution for that star. The wavelengths were then incrementally updated for all other observations of each star using the methods that we describe in Sections 4.2 and 5.2, which are aimed at minimizing systematics in the wavelength solutions from one observation to the next. A total wavelength span of 6519–10 252 Å is covered by the EEV and MITLL chips at the non-standard 840 nm setting of UVES. An order that falls between the two CCDs cannot be used and must be accounted for correctly in the two-dimensional solution. The candidate ThAr lines were subjected to a two-dimensional fit of wavelength versus extracted order (cross-dispersion) for each CCD independently. For each star, an arbitrary reference solution with a two-dimensional polynomial fit using four coefficients in the wavelength direction and six coefficients in the cross-dispersion (order) direction was made:

$$\lambda(x, y) = \sum_{i=0}^{3} a_i x^i \sum_{j=0}^{5} b_j y^j, \quad (1)$$

where *a* and *b* are the polynomial coefficients that we fit for. *x* and *y* are the pixel number and order number, respectively, and *i* and *j* are the powers in *x* and *y* for each coefficient. By iteratively rejecting outlying pixels from the fit, we found that of the input 573 lines, clipping the furthest outliers yielded the most consistent fit from one solution to the next. Typically, 15–20 lines were rejected before a final fit was produced for each observation. The zero-point rms (i.e. the rms by combining all lines) for the *master wavelength calibrations* is found to be $\sim$5–5.5 and $\sim$6–6.5 $m\,s^{-1}$ for the EEV and MITLL chips, respectively, and represents the goodness of fit of the polynomial. These values are dominated by a systematic difference between the wavelengths and the two-dimensional fit. The *variability in the wavelength solution* for a given set of RV measurements (i.e. for each star) is thus important and ultimately determines the precision that can be achieved. We discuss this further in Section 5.2, but note here that this variability is an order of magnitude smaller (i.e. $<1\,m\,s^{-1}$) than the zero-point rms values quoted above.

The appropriate wavelength solution for each observation can be obtained through a *simultaneous* measurement, by using the telluric lines, or a *near-simultaneous* measurement by using the nearby ThAr reference frame. In each instance, the corrections are determined as pixel shifts and applied to the master wavelength solution. This procedure enables wavelength corrections to be applied, allowing for low-order shifts and stretches (due to mechanical effects and temperature/pressure changes). In other words, allowing more degrees of freedom for each solution can lead to poor fits in the first and last orders, near the order edges, and in regions where there may be fewer lines. Low-order corrections correctly describe the changes in the instrument while minimizing variability in the fits. We describe the two methods adopted in this paper for updating the wavelength, using telluric lines (Section 4.2) and ThAr lines (Section 5.2).

4 TELLURICS AS A WAVELENGTH REFERENCE

The benefit of utilizing telluric lines to obtain a local wavelength solution is that the wavelengths are derived from the very observation of the star itself and are therefore simultaneous. The telluric spectrum essentially follows the same light path as the star through the Earth's atmosphere, the telescope and the spectrograph, and is thus subject to the same systematics. The calibration procedure could be seen as analogous to that first adopted by Marcy & Butler (1992) and Butler et al. (1996) if the atmosphere of the Earth could be well characterized and calibrated for. In addition, at the time of observations, there were no optical 8 m class spectrometers that enable simultaneous ThAr observations to be made.

[2] http://starlink.jach.hawaii.edu/starlink

The stability of telluric lines as reference fiducials has been investigated by a number of authors. Griffin & Griffin (1973), for example, made some initial attempts to identify lines in the 6841–7424 Å region, estimating uncertainties at the 1–2 mÅ level, equivalent to ∼40–90 m s^{-1}. The most complete list of ab initio line strengths and positions for water has now been calculated by Barber et al. (2006) and is now routinely used in model atmosphere data bases that supply molecular information for many molecules (Rothman et al. 2009). Bands of telluric molecular absorption lines pose a challenge for any ground-based observations and are seen from the mid-optical, becoming stronger and wider into the infrared. In the red-optical, at wavelengths greater than 6500 Å, significant O_2 absorption bands with bandheads at ∼6865 and ∼7595 Å appear, the latter showing strong absorption with saturation in some lines. H_2O bandheads at 6450, 7170 and 8100 Å exhibit increasing widths from ∼100 Å to several 100 Å; however, the band covering 8890–9950 Å is by far the most extensive at wavelengths short of 1 μm. Gray & Brown (2006) were able to achieve empirical precisions of ∼25 m s^{-1} using strong H_2O absorption lines in the 6222–6254 Å region formed in the optical path of the coudé échelle spectrograph used. This procedure had the advantage of minimizing atmospheric projection effects such as change in airmass.

Figueira et al. (2010) instead took advantage of night-long observations made on bright stable stars with the HARPS, located at the ESO 3.6 m at La Silla. They found clear nightly trends of the RV variations of the O_2 absorption band as measured in the spectra of τ Ceti (HD 10700), μ Ara (HD 160691) and ϵ Eri (HD 20794). Empirical fits were made to the velocities using a simple model that included a linear airmass term (fixed, with magnitude of ∼ 20 m s^{-1}), a projection of the wind velocity along the line of sight of the telescope (encompassing both magnitude and direction) and a fixed calibration offset term. Such a procedure enabled typical measurement precisions over week-long time-scales of 4.5–10 m s^{-1} to be made for observations at less than 1.5 airmass (>41°.8) and 2.4–4 m s^{-1} when restricting observations to less than 1.1 airmass (>65°.4). Over a period of 6 years, the precision was found to be of the order of 10 m s^{-1}.

4.1 Precision RVs of Proxima Centauri

The opportunity to study the stability of telluric lines alone for updating the wavelength solution and providing a stable cross-correlation reference against which to make precision RV measurements is afforded by the archival observations of Proxima Centauri, already outlined in Section 2.2 and initially published in Fuhrmeister et al. (2011). We intended to characterize the stability and behaviour of UVES for our RV measurement technique by making use of the ∼560 archival observations taken over three nights, with an intention of extending the method to our ROPS sample. In addition, this kind of study is not possible with our 2012 July observations since we only observed each target once per night, which precludes monitoring stability on minute- to hour-long time-scales. Kürster et al. (1999) showed that Proxima Centauri is stable to the 54 m s^{-1} level, while more recent results from Endl & Kürster (2008) have shown it to be stable to 3.11 m s^{-1} over a 7 yr period, but quote an average propagated uncertainty of 2.34 m s^{-1} in their measurements, indicating an additional unaccounted for source of noise.

The seeing variations of 1.4 arcsec at high airmass, down to ∼0.6 arcsec at low airmass, when viewed with a 1 arcsec slit offer a less than ideal match since the star does not completely fill the slit. This results in changes in illumination of the échelle, leading to RVs that can potentially vary at the m s^{-1} to several tens of m s^{-1} level. Since the CCD readout was binned by a factor of 2 in the wavelength direction, the mean pixel increment of 2.4 km s^{-1} is twice that of the full 1.2 km s^{-1} mean readout increment used for the ROPS targets. Only one ThAr frame per night was recorded during the automated calibration procedures executed by UVES each night. As a result, it is impossible to track any drift of the spectrograph through the night, or in this instance, to investigate our ability to use the ThAr frames as a near-simultaneous reference fiducial. During extraction, we also discovered that on 2009 March 10 and 14, a regular half hour, cyclic shift of the order of 1 km s^{-1} appears in the RVs. The origin of this cyclical behaviour is unclear, but it appears to coincide with times at which the seeing was very good. We believe that it is related to the mismatch of seeing and slit width where the autoguider may have been fooled into making only occasional corrections that have resulted in significant échelle illumination change.

4.2 RV measurement procedure

Starting with the two-dimensional wavelength solution described in Section 3.1, a method of updating the local wavelength solution for each observation must be obtained. No special wavelength calibrations were made during the observing sequence of Proxima Centauri, and only one ThAr spectrum was recorded during the standard calibrations for each night. We therefore investigated the use of the abundant H_2O and O_2 in the red-optical to update the wavelength solutions.

The weather conditions on the first night were particularly dry, with relative humidity variations in the 2–14 per cent range (as recorded for the telescope dome in the observation headers). On the second and third nights, the relative humidity varied in the ranges 48–54 and 22–28 per cent. The increased water column is clearly evident in the H_2O lines as illustrated in Fig. 1. This additionally serves to illustrate why the use of water lines for precision RV work can prove challenging. With careful selection, it is in fact possible to select H_2O lines that are not blended with other lines and that also do not vary so greatly in strength as to become insignificant relative to the continuum level noise. Since Fig. 1 illustrates the extremes of the telluric line variations during the Proxima Centauri

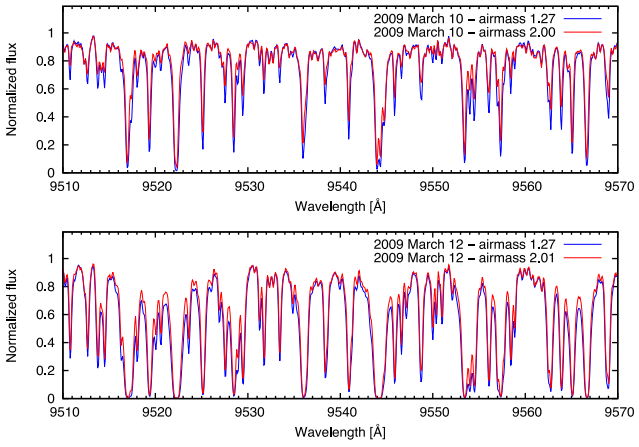

Figure 1. Spectral region 9510–9570 Å illustrating the change in humidity between 2009 March 10 (low humidity: 2–14 per cent) and 2009 March 12 (high humidity: 48–54 per cent) at Paranal. Note that some lines become strongly saturated when the humidity levels are high. Even those lines that do not saturate are highly variable in strength, with some lines (e.g. 9550–9551 Å) almost disappearing.

observations, we found that the optimal procedure was to manually select the appropriate lines that fit these criteria. Over the 0.65–1.025 μm interval, an initial list of tellurics comprising ∼1700 lines, with normalized line depths in the range 0.1–1.0, results in a subset of only ∼300 non-blended H_2O and O_2 lines with normalized lines in the 0.6–0.95 range. Changes in instrumental resolution are likely to affect the selection, with the expectation that more lines could be used with a higher instrumental resolution.

Despite selecting only the strongest unblended H_2O lines, we found that the most stable procedure entailed utilizing *only* the O_2 lines that are recorded in two bands on the EEV chip. The use of O_2 lines was advocated and adopted by Figueira et al. (2010) since they are more stable than H_2O lines which occur in a very narrow layer and are highly variable, being correlated with weather and humidity patterns. We thus made use of only the orders recorded on this chip for the Proxima Centauri data set, which span 6519–8313 Å. Since the two O_2 bands span five orders in total, with some lines recorded twice, we make use of the full information by determining the shift of every recorded instance of each line. A mask is made, to include all the O_2 lines within to 4 FWHM. Only these lines are used to determine the transform.

We found that the most reliable procedure for updating the wavelength solutions via telluric lines is to calculate the transform that maps the reference spectrum to each individual observation in turn. The normalized master spectrum t_j is thus scaled to the current normalized observed spectrum s_j by minimizing the function

$$\chi^2 = \sum_i \left(\frac{s_i - (\xi_0 + \xi_1 t_i + \xi_2 t_i^2)}{\sigma_i + \tau_i} \right)^2, \quad (2)$$

where

$$f_i = \xi_0 + \xi_1 t_i + \xi_2 t_i^2 \quad (3)$$

is the transformed normalized master spectrum, and ξ_1, ξ_2 and ξ_3 are the quadratic transform coefficients for each O_2 line pixel, i, designated by the mask. σ_i and τ_i are the uncertainties on the observed spectrum and the master spectrum, respectively. This procedure is implemented such that all mask designated lines are fitted simultaneously. In other words, the same transform can be applied to all orders to update the wavelength solution. Since ξ_1, ξ_2 and ξ_3 are in pixel units, the wavelength increment per pixel is calculated from the master wavelength frame for all pixels over all the orders used for determining RVs. The master wavelength increment map is multiplied by the pixel increments and added to the master wavelengths to update the wavelength solution.

As in B12, we carry out a least-squares deconvolution using line lists that represent both the telluric line and the stellar line positions. We use the Line By Line Radiative Transfer Model (LBLRTM) code (Clough, Iacono & Moncet 1992; Clough et al. 2005) to obtain telluric line lists, while we derived the stellar line lists empirically. In the latter case, we used high-S/N observations of GJ 1061 made with a 0.4 arcsec slit. The GJ 1061 line list was used for deconvolution of the M5V–M7V targets. For the M7.5V–M9V targets, we used the spectra of LHS 132 (aligned and co-added to augment the S/N ratio). The procedure for derivation of the stellar templates used in this paper is given in Appendix A. Two high S/N ratio lines are thus calculated for each spectrum, with the final velocity calculation being made by subtracting the telluric line position from the stellar line position (measured via cross-correlation).

4.3 RV stability of Proxima Centauri

The RVs for the three nights are shown in Fig. 2. All RVs presented in this section are listed in Table A1. There is a clear trend during each night and an offset, particularly when the first night is compared with the second and third nights. Both the slope curvature and offset

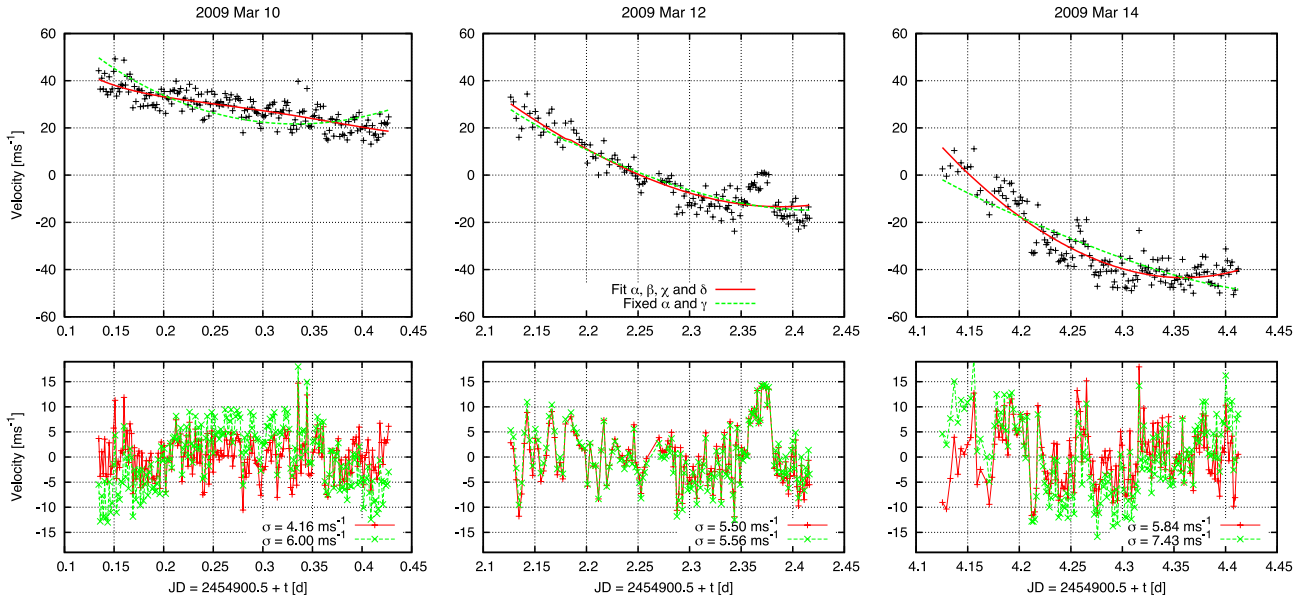

Figure 2. RVs of Proxima Centauri for observations made on 2009 March 10, 12 and 14. The top panels show the heliocentrically corrected RVs on each night along with the fits which account for changes in airmass, wind velocity, direction and offset. The solid/red lines indicate the fits made to each night individually while the green/dashed lines are for fits made with fixed $\gamma = 17.75$. Seeing effects in the 1 arcsec slit, which varied between a maximum of 1.4 arcsec at high airmass and a minimum of 0.6 arcsec at low airmass, were not accounted for during the modelling. The residuals are plotted in the bottom panels (line type and colour correspond to the top panels). The nightly subtracted residuals vary between 4.16 and 5.84 m s^{-1}, while the corresponding $\gamma = 17.75$ fit residuals give rms values of 5.56–7.43 m s^{-1}.

change from night to night. We have used the empirical procedure outlined in Figueira et al. (2010) to model the trends seen in the RVs on each night. The RV correction

$$\Omega = \alpha \left(\frac{1}{\sin(\theta)} - 1 \right) + \beta \cos(\theta) \cos(\phi - \delta) + \gamma \quad (4)$$

was shown to be sufficient to adequately remove atmospheric effects. The parameters α, β, γ and δ can be determined when observations are made throughout the night at the telescope elevations (θ) and azimuth angles (ϕ) of a fixed target. α represents the linear RV drift per airmass ($1/\sin(\theta)$) due to changes in the line shape as different layers of the atmosphere are sampled. β is effectively the wind speed at the time of the observation and δ is the wind direction. γ is an additional offset term that describes the offset of the observations from zero, when all other terms are zero; in our case, this is the heliocentric velocity correction. We have enabled all parameters to be fitted in order to optimize the fit for each individual night. After subtracting the nightly fits, the residuals yield rms values of $\sigma = 4.16$, 5.50 and 5.84 m s^{-1} on each of 2009 March 10, 12 and 14, respectively (Fig. 2). See also Table A1 for a list of all corrected velocities (column 4, titled 'I corr'). These values appear reasonable considering the expected Poisson-limited S/N of $\sim$2 m s^{-1} (Barnes et al. 2013). From previously unpublished archival HARPS data[3] and UVES observations (Zechmeister et al. 2009), we find the RV of Proxima Centauri to show rms scatter at the 2.3 m s^{-1} (27 observations) and 4.3 m s^{-1} (339 observations) levels, respectively (Tuomi et al., in preparation).

The typical wind speed values we determine (130, 150 and 190 m s^{-1} for each night) are large and potentially not physically realistic. In addition, we find respective values for α, the variation per airmass, of 31, 11 and 23 m s^{-1} while the value of γ varies between -169.1 and 100.9 m s^{-1} (i.e. 270 m s^{-1} variation). As noted by Figueira et al. (2010), γ and α should be fixed. However, the observations are not ideal, with varying humidity [see Gray & Brown (2006) for a discussion of temperature, pressure and humidity effects, which can reach km s^{-1} levels]. The additional problems with the cyclical behaviour during good seeing and the apparent trend of uncorrected RV drift with seeing, especially when the seeing FWHM falls in the 0.6–0.8 arcsec range in the 1 arcsec slit, are likely to yield systematics. For this reason, we believe that the data are not able to reliably constrain wind speed values and directions for the Proxima Centauri observations, unlike the highly stabilized HARPS observations of τ Ceti. Nevertheless, by holding γ fixed at the mean velocity (for the three nights) and fixing the 17.75 m s^{-1} value for α found by Figueira et al. (2010), the corresponding corrected RV rms values for each night are $\sigma = 6.00$, 5.60 and 7.43 m s^{-1} on March 10, 12 and 14, respectively. The corrected velocities using this procedure are listed in Table A1 (column 5, titled 'A corr'). More reasonable wind speeds of 115, 74 and 53 m s^{-1} are found, but again we stress that these are probably biased by the unconstrained effects discussed above. Most notably, the curvature is not fitted well in these fits (Fig. 2, green curves in the upper panel) indicating the probable involvement of seeing variations. For comparison, when considering the data taken with an airmass range up to 1.5, Figueira et al. (2010) found rms scatter of between 4.54 and 5.81 m s^{-1} for τ Ceti (G8.5V) using the same method as described here. The RV of τ Ceti is known to be very stable with a standard deviation of 1.7 m s^{-1} (Pepe et al. 2011).

[3] http//archive.eso.org/eso/eso_archive_main.html

4.4 Concluding remarks

The study in this section was motivated by a desire to characterize a *simultaneous* reference fiducial in order to obtain a local wavelength solution for our deconvolution procedure. With a few caveats, we are able to reproduce similar precision with an M6V star (Proxima Centauri) to that achieved with a G8V star (τ Ceti) with HARPS. Undoubtedly, a stabilized spectrograph, a narrower slit (or at least a slit width well matched with the median seeing) should remove some of the additional trends in the data that equation (4) cannot describe. Despite these promising findings, the major drawback of this procedure is that regular observations of a single target throughout each night would be necessary for successful implementation. We would never realistically expect to observe a given target at such a range of airmasses, and indeed Figueira et al. (2010) found that restricting observations to a narrower airmass range was necessary to achieve the precisions reported.

Given that the trends throughout each night are also approximately linear or quadratic, correcting for atmospheric effects with a four-parameter fit such as equation (4) clearly requires very high S/N ratio. Obtaining few m s^{-1} precision via this method has been possible for Proxima Centauri observations that enable S/N ratios of a few hundred. However, typical observations of late M stars will only achieve S/N ratios of several tens, which will more severely restrict the precision achievable. Internal calibration references are therefore always a preferred and more realistic option for obtaining the local wavelength solution for deconvolution. We thus subsequently adopt this procedure for our ROPS sample of late M dwarfs, described in the following sections.

5 UVES OBSERVATIONS OF A LATE M DWARF SAMPLE

For the late M stars observed with UVES, our strategy comprised of observing the same sequence of 15 targets during each of four half nights. The observations were made over a 6 d period on 2012 July 23, 24, 26 and 29. This enables a time span that is sufficient to discern short-period signals of the order of a few days. Since we are unable to implement the procedure described in the previous section, which made use of the telluric lines to update the wavelength solution for deconvolution of each spectrum (see Section 4.4), we used the near-simultaneous ThAr frame recorded after each observation as a local wavelength solution.

5.1 RV stability of UVES

In B12, we determined an incremental drift relative to a reference wavelength solution in order to obtain the local wavelength solution in each order. The MIKE spectrograph however exhibited shifts of up to a few hundred m s^{-1} over short time-scales, which we attributed to mechanical stability and possible gravitational settling of the dewar as the coolant boils off during the night. UVES appears to exhibit a much more predictable behaviour in that a more monotonic drift in wavelength is seen through a single night, although there is an offset between each night as shown in Fig. 3 (top panels). Again the nightly offset may be related to both dewar refills and to re-configuration of UVES which regularly observes at different wavelengths. Shifts of the order of 50 m s^{-1} can be expected with UVES when different ThAr spectra are taken after changing the

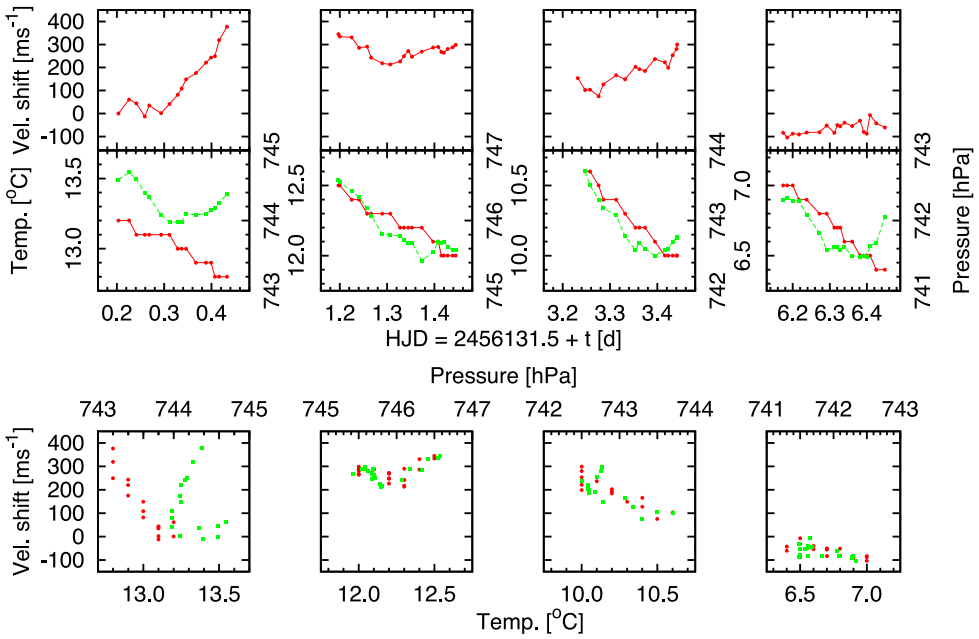

Figure 3. Stability of UVES during observations in 2012 July. The top panels show the drift in m s^{-1} on each night and the middle panels plot the temperature of the red camera. While 0.4–0.6 drift is seen on each night, the absolute temperature values are different. The bottom panels show the drift versus the temperature. Temperatures are plotted as filled red circles (scales on the left and bottom axes), while pressure is plotted as filled green squares (scale in hPa on the right and top axes).

instrument configuration.[4] In addition, shifts of the order of 1/20 pixel per 1 hPa (millibar) change in pressure and the same shifts for a change of 0.3 in temperature are typical. The recorded 0.4–0.6 variation throughout each night (Fig. 1, filled red circles) during our observations would thus lead us to expect a 100–150 m s^{-1} wavelength shift. The pressure drift on each night is of the order of 1 hPa (Fig. 1, filled green squares) and hence presumably contributed to the observed drift. While attributing the observed shifts to temperature changes alone is in agreement with expectation on nights 2, 3 and 4 of our observations, the first night, which was the least humid, showed ∼400 m s^{-1} drift through the night. At the same time, the temperatures were highest on the first night, possibly indicating that drift rate is correlated with temperature. This increased drift rate is discussed later in light of our derived RVs.

5.2 Local ThAr wavelength solution

Subsequent to obtaining a master solution for each star, as outlined in Section 3.1, we have adopted a method for obtaining the local wavelength solution for each frame that is different from that described in Section 4.2, which made use of telluric lines. For our ROPS targets, we obtain the local wavelength frame taken after each observation by instead updating the wavelength positions of all the ThAr lines used to determine the master solution. The pixel positions of all the lines are calculated as outlined in Section 3 before subtracting the line positions of the master wavelength frame. This procedure has the advantage that lower order corrections can then be applied to update the master wavelength solution. A two-dimensional fit is made for pixel position versus order for all the measured pixels. In other words, a two-dimensional pixel shift surface is determined and we find that a polynomial of

[4] http://www.eso.org/sci/facilities/paranal/instruments/uves/doc

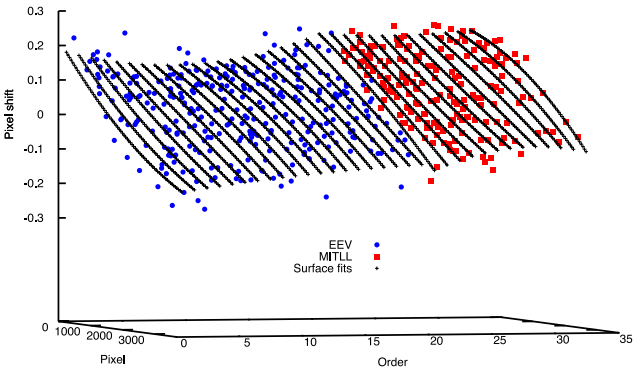

Figure 4. Example of the ThAr line pixel shifts for EEV (blue circles) and MITLL (red squares) CCDs for the 33 extracted orders. The black '+' symbols represent the fitted 3 (wavelength) by 2 (cross-dispersion/order) polynomial surface. Shifts are relative to the master wavelength frame taken with each observation on the second night of observations.

degree 3 (quadratic) in the wavelength direction and 2 (linear) in the cross-dispersion direction (Fig. 4) is sufficient to describe the drifting wavelength solution relative to the master solution which was calculated via a 4 × 6 polynomial (Section 3.1). The fitted pixel shift surface can be written as

$$\Delta p(x, y) = \sum_{i=0}^{2} a_i x^i \sum_{j=0}^{1} b_j y^j, \quad (5)$$

where $\Delta p(x, y)$ is the pixel drift surface defined at each pixel, x, and extracted order number, y. The coefficients a and b scale the x and y terms of power i and j, respectively. The pixel surfaces are converted to an updated wavelength surface by calculating wavelength increments from the master wavelength frame and adding to the master wavelength frame. This procedure has the advantage of maintaining stability as any order edge effects are minimized in a

low-order fit. Zero-point rms values in the wavelength solutions of 2.01 ± 0.20 and $2.63 \pm 0.24\,\mathrm{m\,s^{-1}}$ for the EEV and MITLL chips, respectively, are found. As already noted in Section 3, these values could be reduced by using additional calibration lamps, but we note that the 1σ variability is an order of magnitude lower at 20 and 24 $\mathrm{cm\,s^{-1}}$, and well below the photon-noise precision that can be achieved with UVES using the techniques described in this paper.

5.3 RVs of 15 late M dwarfs

The mean-subtracted RVs for our ROPS targets are plotted in Fig. 5 with details of rms estimates listed in Table 1. Appendix A gives full details of all RVs, which are listed in Tables A2 and A3. The RVs are measured as outlined in B12 by subtracting the deconvolved telluric line position from the simultaneously observed stellar line. The line positions are measured by cross-correlating each stellar line relative to the mean deconvolved stellar line for each target, and similarly for the telluric lines. We use the HCROSS algorithm of Heavens (1993) which is a modification of the Tonry & Davis (1979) cross-correlation algorithm. HCROSS utilizes the theory of peaks in Gaussian noise to determine uncertainties in the cross-correlation peak. We have made a minor modification of the routine, which belongs to the Starlink package, FIGARO, in order to directly output both the pixel shift and shift uncertainty.

From Table 1, it can be seen that a range of exposure times and S/N values were obtained, depending on the brightness of the target, which ranged from $m_I = 9.5$ to 14.1. In addition, not all observed targets possess slow rotation, which we define as at or below the instrumental resolution of 54 000 or $5.55\,\mathrm{km\,s^{-1}}$. Jenkins et al. (2009) found that M6V stars possess $v \sin i = 8\,\mathrm{km\,s^{-1}}$ on average, while this increases to $\sim$15 $\mathrm{km\,s^{-1}}$ for M9V. Table 1 and Fig. 5 demonstrate that those stars with slower $v \sin i$ values on the whole appear to enable better RV precision to be determined, as first noted by Butler et al. (1996). This is not surprising since the resolution is effectively degraded and line blending increases with increasing $v \sin i$. The correlation between photon-limited precision and rms *for a given* $v \sin i$ was also simulated in B12 and Barnes et al. (2013), and we further discuss and illustrate the 'excess' rms (i.e. above that expected from $v \sin i$ and S/N ratio alone) in Sections 5.4 and 5.5.3 and Fig. 8.

For the early M dwarf sample targeted by HARPS, Bonfils et al. (2013) found an anticorrelation when plotting bisector spans (BIS) against the measured RVs. For instance, a clear correlation (with a Pearson's correlation of $r = -0.81$) was identified for Gl 388 (AD Leo). Subtraction of the trend decreased the rms from 24 to $14\,\mathrm{m\,s^{-1}}$. We have calculated the BIS (Gray 1983; Toner & Gray 1988; Martínez Fiorenzano et al. 2005) for all our stars and subtracted the best-fitting linear trend with the derived RVs. The uncorrected RVs are listed in column 9 of Table 1, while the BIS-corrected RVs are listed in column 10 and show that a number of our stars also demonstrate trends that are linked with the line bisector span (BIS). These stellar line BIS-corrected velocities and subsequent rms values are plotted in Fig. 5, and we refer to these corrected values in the following discussion. Significant improvements in the rms are seen for a number of targets, where the rms is halved. The corrected RVs however show little improvement in the stars that exhibit the largest $v \sin i$ and derived rms values. Improvements are also seen if a correlation with the telluric BIS is removed (column 11), indicating that atmospheric variation may also contribute to limiting the precision that can be achieved using the methods outlined above. Also, variability in the slit illumination (e.g. due to seeing changes) affects the instrumental point spread function, thus affecting both stellar and telluric lines to some degree. This will go some way to explaining why stellar or telluric lines can improve the measured rms. However, only the stellar lines contain line shape variability introduced by the star itself. Finally, we have also investigated incorporating both the line and telluric BIS measurements. Since the final RVs are measured by subtracting the telluric line position from the stellar position, we also list RV-BIS corrections for a stellar–telluric BIS correction (column 12).

5.4 Discussion

The rms velocities demonstrate that near-photon noise-limited precision is achievable using our red-optical survey. Following B12, where photon-noise-limited simulations were made with the MIKE spectrograph at the 6.5 m Magellan Clay telescope, we have estimated that 1.5–2 $\mathrm{m\,s^{-1}}$ should be achieved with UVES (Barnes et al. 2013). The observations, in particular for GJ 1061, GJ 1002 and 2MASS J03341218−4953322 (Table 1) thus show considerable improvements over recent measurements that have made use of telluric lines as a reference fiducial (e.g. Reiners 2009; Bailey et al. 2012; Rodler et al. 2012). The BIS-corrected 2.4, 5.1 and 6.4 $\mathrm{m\,s^{-1}}$ measurements for these objects compare favourably with those that we obtained with HARPS for the brightest targets in our sample. While GJ 1061 and GJ 1002 have not been actively monitored with HARPS, four observations for each target (that remain unpublished) exist in the ESO's archive. Using TERRA, the Template-Enhanced Radial velocity Re-analysis Application (Anglada-Escudé & Butler 2012), a pipeline suite designed to improve the RVs achieved by the standard HARPS Data Reduction Software, we have found 2.04 and 2.32 $\mathrm{m\,s^{-1}}$ precisions for GJ 1061 and GJ 1002 (see Table A4 for RVs). We note that only the reddest orders of HARPS in the very brightest mid-M targets enable precision of a few $\mathrm{m\,s^{-1}}$ to be achieved.

Despite the sub-10 $\mathrm{m\,s^{-1}}$ rms values, a number of our stars exhibit RVs that are significantly in excess of the photon-noise-limited precision that we expect from our targets, even when $v \sin i$ is taken into consideration. The RVs for the less stable targets indicate that rotation and activity may play a role in the observed larger rms values. As the average M6V star exhibits $v \sin i = 8\,\mathrm{km\,s^{-1}}$ (Jenkins et al. 2009), we expect velocity precisions of $\sim$10 $\mathrm{m\,s^{-1}}$ for S/N = 30 (Barnes et al. 2013). However, while we predict photon-noise-limited precisions of 13, 15 and 20 $\mathrm{m\,s^{-1}}$ for GJ 3076, LP 759-25 and LP 412-31, respectively, they exhibit RVs that are an order of magnitude higher. The uncorrected RV values for these targets are also not significantly improved (at least relative to the photon-limited precision) when we include BIS corrections with the stellar lines or telluric lines. The best improvement is seen for the combined stellar and telluric line correction. While it is possible to select stellar lines for deconvolution that are free of any significant telluric lines (i.e. we use regions free of telluric lines with depths $>$0.05 of the normalized continuum), it is conversely not possible to select telluric line regions that are free of stellar lines. Any cross-contamination of the tellurics is thus more likely if the stellar lines show signs of activity variability. To ascertain whether the increased rms scatter may be related to stellar variability, in Section 5.5 we investigate spectral lines that are sensitive to chromospheric activity.

5.4.1 *The effect of instrumental drift on RV precision*

The first night of our observations, 2012 July 23, was particularly dry and hence tellurics with smaller equivalent widths (EWs) were

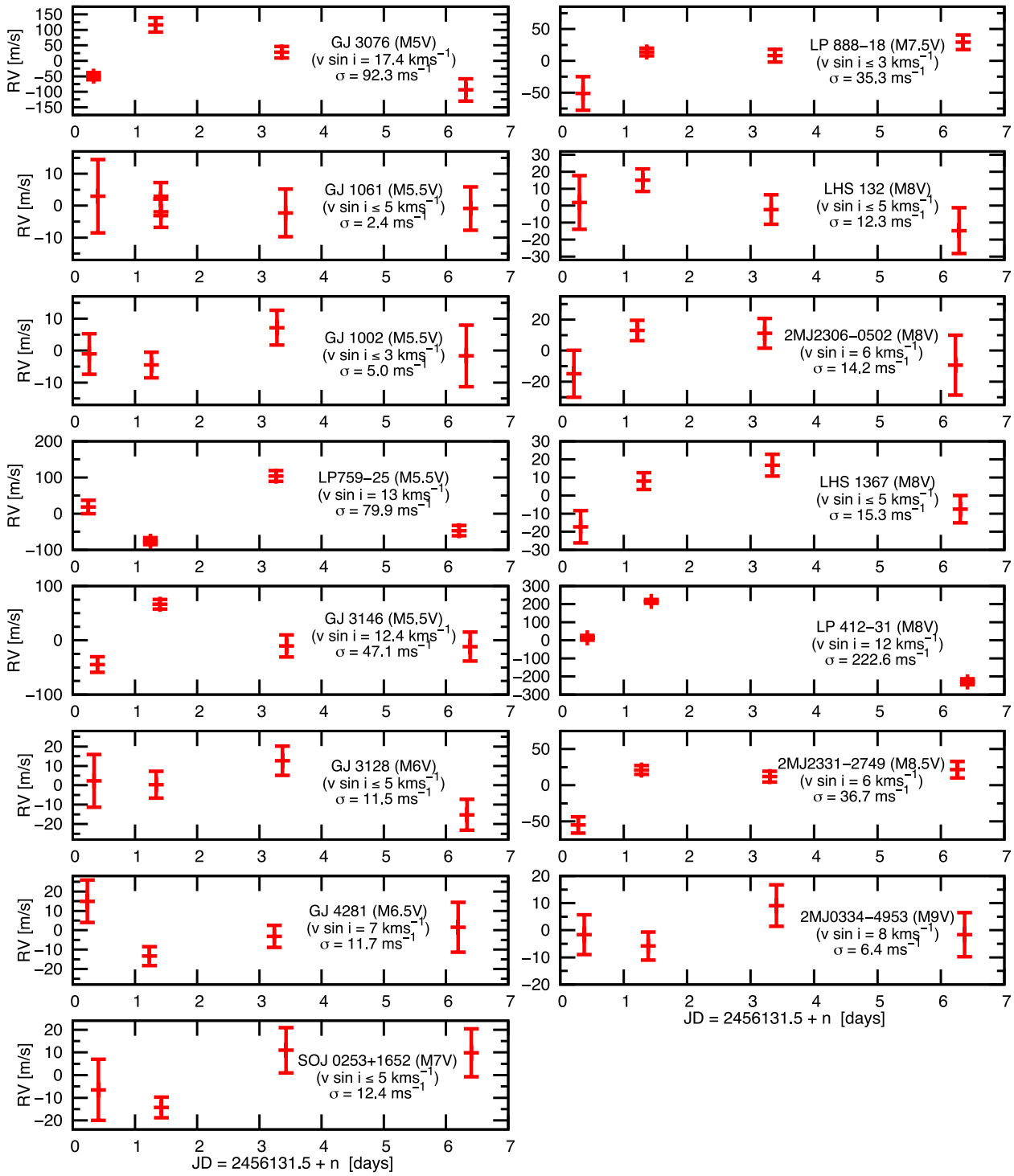

Figure 5. Heliocentrically corrected RVs plotted for our 15 UVES ROPS targets. Observations were made on 2012 July 22, 23, 25 and 28. The sample contains a total of seven M5V–M6.5V and eight M7V–M9V targets. An RV precision of 2.4 and 5.0 m s^{-1} is measured for quiet, slowly rotating targets at spectral type M5.5V (GJ 1061 and GJ 1002), while 6.4 m s^{-1} is found for our latest, M9V, target (2MASS J03341218−4953322). The targets showing higher rms in Table 2 either exhibit significant rotation ($v \sin i \gtrsim 10$ km s^{-1}), significant variability in the chromospheric indicators, Ca II and Hα or both.

derived, leading to RVs with larger error bars. Fig. 3 also shows that the largest drift rates were observed with UVES on the first night. Those targets that were observed during the highest rate of drift appear to show RV measurements with the greatest offset on each night. One might expect an improved velocity precision if each stellar observation were bracketed by ThAr observations, which would enable interpolation of the wavelength scale to the time centroid of the observation. Applying this procedure did not significantly improve our rms precision however, probably because the preceding ThAr was taken *before* the telescope was slewed to the new object. Unlike properly stabilized and fibre-fed instruments UVES is located at one of the Nasmyth foci and is thus potentially subject

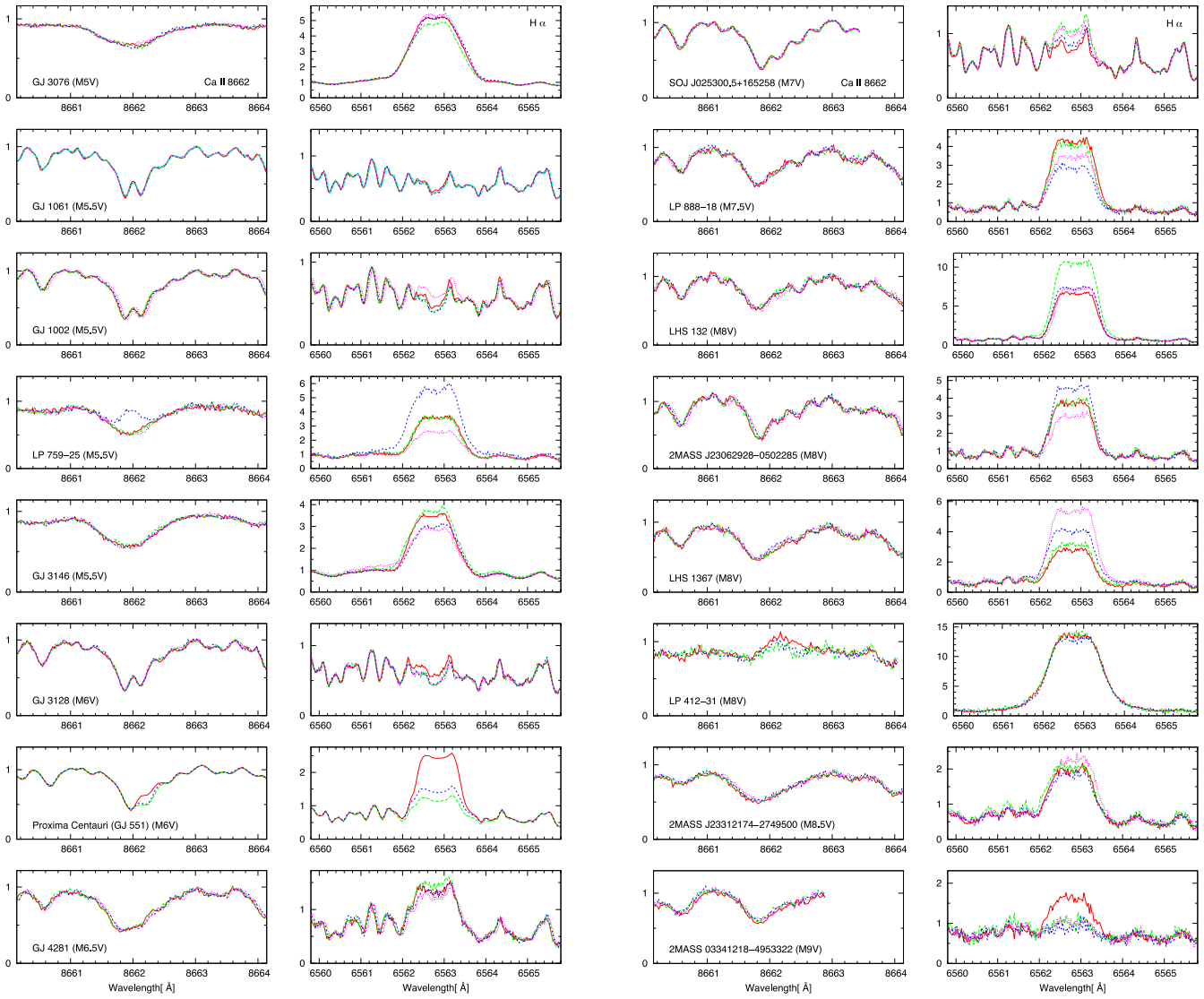

Figure 6. The Ca II 9662.14 Å profiles (left) and corresponding Hα (6552.80 Å) lines (right) for all observations of the 15 ROPS targets listed in Table 1. For each target, the matched colour is used to signify that the Ca II 9662.14 Å and Hα lines were extracted from the same spectrum. We have also included profiles from the Proxima Centauri data set for the minimum, maximum and mean Hα emission and corresponding Ca II 8662.14 Å levels. The plotted wavelengths span 4 Å for Ca II and 6 Å for Hα. The blending of the Ca II 8662.14 Å profile with the nearby Fe I line at 8661.90 Å is clearly seen in the slower rotating, earlier stars in the sample (e.g. GJ 1002, GJ 1061 and GJ 3128). 2MASS J03341218−4953322 possesses a large RV (see Appendix A, $\Gamma_{\rm 2M\,J03\text{-}49} = 73\,732.21\,{\rm m\,s^{-1}}$), and since the Ca II line is located near the edge of the order, the spectrum appears truncated when the line is re-centred to 8662.14 Å.

to vibration and centripetal forces through slewing of the telescope from one target to the next. It is not clear whether movement of the telescope is able to affect the drift rate, but it does not necessarily appear to result in random changes in the drift *direction*. Bracketing every science exposure with ThAr exposures (i.e. immediately before and after the observation), *with the telescope at fixed Right Ascension and Declination*, is likely to enable further improvements in RV precision. This procedure will be adopted with any future observations.

5.5 Chromospheric activity

The degree of stellar variability, as measured from chromospheric activity indicators in our target sample, varies considerably. While some of our more RV-stable targets such as GJ 1061 and GJ 1002 show low levels of chromospheric activity (e.g. flaring), others at similar spectral type and activity levels, such as Proxima Centauri, show higher levels of variability in lines such as Hα. The degree to which chromospheric activity significantly impacts upon measured RVs is not well known for mid-to-late M dwarfs. Reiners (2009) found that the flaring activity, with 0.4 dex variability in Hα for the mid-M star, CN Leo, did not result in RV deviations at the $10\,{\rm m\,s^{-1}}$ level, although a large flare event in that study did result in an RV deviation of several hundred $\rm m\,s^{-1}$. The impact and correlation of activity variability with measured RVs in our ROPS sample are investigated in the following sections.

5.5.1 Hα as an activity indicator

In order to monitor the chromospheric activity of each star (i.e. presence of active regions and flaring events), we have examined the Hα line, which is plotted for all observations in Fig. 6 (the

Ca II 8662.14 Å line, also plotted, is discussed in Section 5.5.4). In the case of Proxima Centauri, we plot the minimum, mean and maximum Hα emission since there are a total of 561 observations in the 2009 data set.

We have estimated the activity in our ROPS sample, by calculating Hα emission for all observations of each target. The Hα emission in each spectrum was calculated by measuring the EW of the line. We adopted the procedure described in West et al. (2004), by measuring the EW(Hα) relative to the normalized continuum. Following West & Hawley (2008), the continuum regions are defined as 6555–6560 and 6570–6575 Å. Several of our targets, GJ 1061, GJ 1002 and GJ 3128, have some or all measurements that yield negative EWs since the local continuum level is difficult to measure when Hα is barely visible. We have therefore assumed that all measurements are relative to the lowest measured EW which we assume is limited by the calculated EW uncertainty, as measured from the variances propagated during extraction. For any star with a significant emission EW, this uncertainty is negligible. Using flux-calibrated spectra from nearby M stars, West & Hawley (2008) estimate χ values, the ratios of continuum flux around Hα to the bolometric flux. Using their tabulated values of χ for Hα, we can determine $F_{\rm H\alpha}/F_{\rm bol} = L_{\rm H\alpha}/L_{\rm bol} = \chi({\rm H}\alpha)\ {\rm EW(H}\alpha)$. The same procedure was adopted by Mohanty & Basri (2003) who instead of using flux-calibrated observations relied upon the models of Allard et al. (2001) to estimate χ. Luminosities are presented in the form, $\log_{10}(L_{\rm H\alpha}/L_{\rm bol})$, which are given for each star in Table 2. It is immediately evident that the majority of stars show some degree of variability. Visual representations of the Hα variability as a function of both spectral type and $v \sin i$ are shown in Fig. 7.

For the most stable star in the sample, GJ 1061, Hα is barely discernible, with variability of ∼4 per cent of the normalized continuum. Both GJ 1002 and GJ 3128 show Hα that is also filled in but with variability at the 20 per cent level. On the other hand, the M6.5V to M9 targets all show Hα in emission that varies considerably (see values in Table 2). The notable targets, however, are those exhibiting significant rotation, with Hα in strong emission, namely LP 412-31, GJ 3146, LP 759-25 and GJ 3076. These targets possess the highest rotation in our sample, with $v \sin i$ values of 12, 12.4, 13 and 17.1 km s^{-1} respectively. GJ 3076 shows the least variability, indicative of saturation, while LP 412-31 (with the highest measured EW) is also only moderately variable. Bell et al. (2012) also made this observation for the complete M spectral range (M0V–M9V). They attributed this phenomenon to the higher level of persistent emission requiring significant heating (flaring) events to give a measurable change in emission.

Mohanty & Basri (2003), West et al. (2004) and more recently Reiners & Basri (2009, 2010) have studied rotation and activity across the M dwarf spectral class. By observing large samples, these studies indicated trends with chromospheric activity and $v \sin i$. West et al. (2004) studied 8000 spectra of low-mass stars from the Sloan Digital Sky Survey and found that 64–73 per cent of M7V–M8V stars were active. Here, although our sample is small, we see considerable variability in any specific object. Hence, for the more active targets, a single snapshot observation is not necessarily representative of the mean activity level for that particular star. The trend first noted by Mohanty & Basri (2003) and further quantified in Reiners & Basri (2010) suggests that Hα emission occurs at lower rotation rates in the later M stars. This is also apparent in our sample, where the M5V–M6V targets with slow rotation $\leq$5 km s^{-1} do not on the whole show a strong Hα line, whereas the M6.5V–M8V targets all possess significant Hα emission and variability for the similar rotation velocities. The sudden fall in $L_{\rm H\alpha}/L_{\rm bol}$ noted by Mohanty & Basri (2003) is seen in our latest targets, which despite similar rotation velocities of 6 and 8 km s^{-1} show both the smallest EW$_{\rm H\alpha}$ and $\log_{10}(L_{\rm H\alpha}/L_{\rm bol})$ values. Our findings are thus in keeping with the late spectral type activity frequency plots of Reiners & Basri (2010) (see their fig. 7).

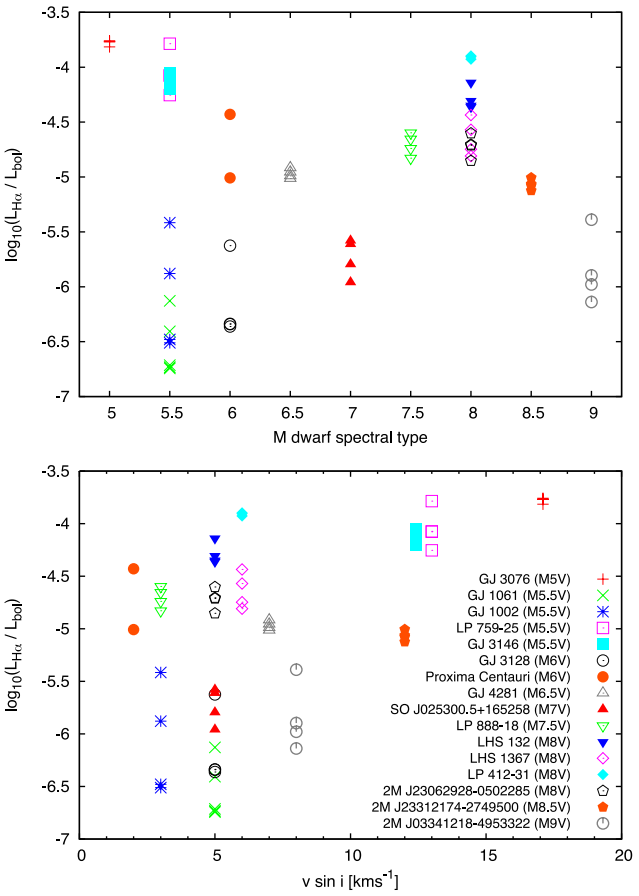

Figure 7. Activity, $\log_{10}(L_{\rm H\alpha}/L_{\rm bol})$, as a function of spectral type (top) and $v \sin i$ (bottom) for the 15 ROPS targets and Proxima Centauri. The symbols and colours for each object are indicated in the lower panel key and apply to both plots. The earliest star with significant rotation exhibits the highest $\log_{10}(L_{\rm H\alpha}/L_{\rm bol})$, while down to M8V, significant activity variation is seen at more moderate rotation speeds. Except for Proxima Centauri, the slowly rotating M5.5V–M6V stars show little Hα activity, while the latest stars in the sample (M8.5V and M9V) are also less active.

5.5.2 *Morphology of Hα emission line*

We make an additional observation regarding the shape of the Hα line, which may be applicable to stars (or subset populations of stars), such as the latest M dwarfs, where Hα is always seen in emission. The exact morphology of the line appears to vary, with the emission profiles for some objects appearing to exhibit more pronounced double-horned peaks than others. Further investigation of the detailed shape of Hα is warranted when it is realized that this shape is typical of emission from time-varying circumstellar material at high stellar latitude. For example, Barnes et al. (2001) observed variability of Hα emission in the low axial inclination G8V α Persei star AP 149, attributing it to a prominence system. A Doppler tomogram, derived using the code developed by Marsh & Horne (1988), enabled four main emitting regions, located at and beyond co-rotation, to be inferred. While this technique requires

Table 2. Hα variability for each object. Minimum and maximum Hα equivalent widths are listed for each object in columns 4 and 5, respectively. The corresponding minimum and maximum $\log_{10}(L_{H\alpha}/L_{bol})$ are calculated from the appropriate models and listed in columns 6 and 7 (see Section 5.5.1).

Star	SpT	$v \sin i$ (km s^{-1})	Min EW (Å)	Max EW (Å)	Min $\log_{10}(L_{H\alpha}/L_{bol})$	Max $\log_{10}(L_{H\alpha}/L_{bol})$
GJ 3076	M5V	17.1	5.59	6.36	−3.81	−3.76
GJ 1002	M5.5V	≤3	0.01	0.17	−6.51	−5.42
GJ 1061	M5.5V	≤5	0.01	0.03	−6.74	−6.12
LP 759-25	M5.5V	13	2.48	7.27	−4.08	−3.79
GJ 3146	M5.5V	12.4	2.80	3.92	−4.20	−4.05
GJ 3128	M6V	≤5	0.02	0.13	−6.36	−5.62
Proxima Centauri	M6V	2	0.56	2.11	−5.00	−4.43
GJ 4281	M6.5V	7	0.85	1.06	−5.01	−4.92
SO J0253+1652	M7V	≤5	0.21	0.51	−5.61	−5.58
LP 888-18	M7.5V	≤3	2.65	4.51	−4.83	−4.60
LHS 132	M8V	≤5	7.25	12.09	−4.36	−4.14
2M J2306−0502	M8V	6	2.34	4.17	−4.85	−4.60
LHS 1367	M8V	≤5	2.59	6.11	−4.81	−4.44
LP 412-31	M8V	12	19.72	21.11	−3.93	−3.90
2M J2331−27495	M8.5V	6	1.53	2.02	−5.12	−5.01
2M J0334−49533	M9V	8	0.19	1.08	−6.14	−5.39

sufficient velocity resolution to enable such a study, asymmetric variability of Hα emission may well be measurable in more slowly rotating stars. We find such variability at the 1–2 per cent level in the Proxima Centauri observations, with a trend suggesting a period that is greater than the 5 d time-scale of the observations. With prolonged monitoring, the rotation period of stars that show Hα in strong emission may thus be estimated, while the exact shape of the emission (the prominence of the horns) may change with inclination angle.

5.5.3 *Hα and $v \sin i$ as a proxies for RV precision in late M stars*

The upper panel of Fig. 8 shows a plot of $v \sin i$ versus rms (stellar line-corrected BIS) values in this paper, illustrating the importance of $v \sin i$ in limiting the attainable precision as might intuitively be expected. We note that 2MASS J03341218−4953322 attains a precision that is greater than photon statistics predict (i.e. lower rms). This is probably a statistical effect that could potentially affect any small sample of observations. The contours plotted in Fig. 8 were estimated by Barnes et al. (2013) using Monte Carlo simulations with an M6V model atmosphere (Brott & Hauschildt 2005), while the increased number of opacities in an M9V star would lead us to expect a lower achievable precision. The Pearson correlation coefficient, r, gives an indication of the correlation. For $v \sin i$ versus rms, we find $r = 0.74$, indicating a strong positive correlation. The slope of the correlation itself is important when using $v \sin i$ as an indicator of expected precision. The discrepancy from the photon-noise-limited precision is greatest for the stars with the highest $v \sin i$ values, as we noted for the most rapid rotators in Section 5.4. Relying on $v \sin i$ to obtain an estimate of rms may therefore lead to an underestimation of the stellar jitter.

In Fig. 8 (middle panel), the spectral type versus rms is plotted. Clearly, the correlation with spectral type is weak, where we find $r = 0.04$. If we instead consider $\log_{10}(L_{H\alpha}/L_{bol})$ as an indicator of rms, as plotted in Fig. 8 (bottom panel), we again see a clear trend. The Pearson correlation coefficients for the lower and upper $\log_{10}(L_{H\alpha}/L_{bol})$ values are $r = 0.76$ and 0.82, respectively. Considering upper and lower limits together, we obtain $r = 0.77$. The significance of the trend of $v \sin i$ versus rms and that of $\log_{10}(L_{H\alpha}/L_{bol})$ versus rms across our sample are thus comparable. It would appear that the absorption lines of late-type stars are significantly affected by magnetic activity, especially when moderate rotation of $v \sin i \sim 10$ km s^{-1} and above is observed. Although relying on $v \sin i$ to estimate rms may underestimate the jitter in this regime, the use of Hα emission level instead removes the rotation dependence.

5.5.4 *Ca II 8662 Å activity and correlation with Hα variability*

The Ca II H&K lines have regularly been monitored in F-M-type stars for many years (e.g. Wilson 1978; Baliunas et al. 1995) since their emission cores show strong variability connected with stellar magnetic activity. The S index measured from the H&K lines (Baliunas et al. 1995) is known to be a general indicator of activity as it is related to the area and the strength of magnetic activity on a star (Schrijver et al. 1989). Stars with low $\log R'_{HK}$ indices (the fraction of a star's luminosity in the Ca II H&K lines) are generally selected for precision RV searches for planets (e.g. Wright et al. 2004). The role of Ca II H&K excess emission and its relationship with jitter in the large sample of the California Planet Search have been studied by Isaacson & Fischer (2010) for instance. In the subset of their sample that includes the latest stars (early M dwarfs), a noise floor is seen with evidence for a trend that increases with activity, as discussed in Section 5.5.3 above.

Although the Ca II H&K lines are very strong and easily accessible for F-K-type stars observed with most high resolution spectrometers, the flux at blue wavelengths, especially by mid-M spectral type, is too low to enable sufficient S/N to be attained during typical observations. Other Ca II lines that are sensitive to chromospheric activity, such as the so-called infrared Ca II triplet, are however observed in the wavelength regime in which our survey operates. Of the infrared Ca II triplet lines at 8498, 8542 and 8662 Å, the latter line appears the least blended. Hence, we chose to illustrate the non-local thermodynamic equilibrium behaviour (i.e. potential emission in the core) of this line in Fig. 6. The line becomes indistinct, through blending with other lines, in the later spectral types in our sample. In our ROPS sample, variability above the noise level can be discerned in Fig. 6, notably for GJ 3076 and LP 412-31. The clearest variation in this line is seen with LP 759-25 (similar

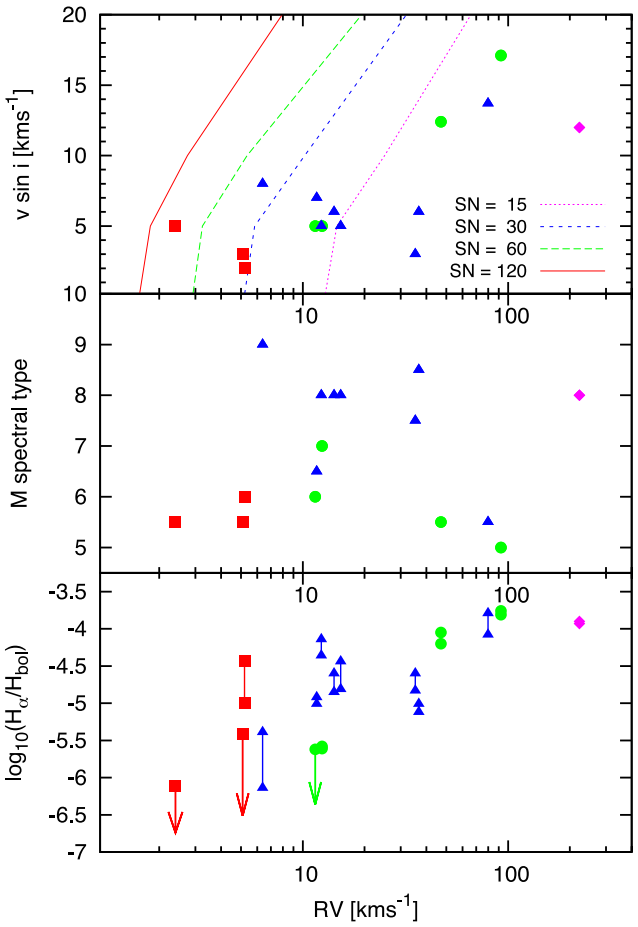

Figure 8. Key stellar parameters plotted against rms (line BIS corrected) for the ROPS targets and Proxima Centauri. The plots are of $v \sin i$ versus rms (top), spectral type versus rms (middle) and activity ($\log_{10}(L_{H\alpha}/L_{bol})$) versus rms (bottom). The symbols and colours used in all panels denote the S/N ratios or S/N ratio intervals for each observed target: $0 \leq S/N < 15$ (red squares), $15 \leq S/N < 30$ (green circles), $30 \leq S/N < 60$ (blue triangles), $S/N \geq 100$ (magenta diamonds). Similarly, photon-noise-limited contours from Barnes et al. (2013) are plotted in the top panel for S/N = 15, 30, 60 and 120, respectively (red/solid, green/long-dash, blue/short-dash, magenta/dotted). The stars with the highest $v \sin i$ values are most discrepant from the photon-noise-limited case, indicating the importance of activity as an indicator of expected precision. Maximum and minimum values of Hα luminosity, as given in Table 2, are plotted as circles connected by a line for each star in the bottom panel. For GJ 1061, 1002 and 3128, very small line EWs were found for some or all (GJ 1061) phases. An arrow head indicates that the lowest Hα luminosity is a sensitivity limit, and equal to the EW uncertainty.

variability is also seen, but not plotted, in the other two infrared Ca II lines).

It appears that variability in the Ca II 8662 Å line is only easily discerned for very strong flares. Fuhrmeister, Liefke & Schmitt (2007) observed the behaviour of the Ca II triplet lines for the flaring M5.5 dwarf CN Leo, noting the correlation with other chromospheric lines. In the case of Proxima Centauri, Fuhrmeister et al. (2011) presented UVES observations of Ca II H&K, Hα alongside optical light curves (obtained with the blue exposure meter of UVES). The Ca II triplet lines were not discussed in their study; however, simultaneous observations with *XMM–Newton*, covering the 0.2–10 keV range and the *U* band (300–390 nm), were presented. We have also included Hα and Ca II 8662 Å in Fig. 6 to demonstrate the range of variability seen over all observations of the 2009 data. Profiles are included for the minimum, mean and maximum states, with the latter corresponding to the strongest flaring event on the final night. Although the correlation between Hα variability and the infrared Ca II triplet variability was not included in the study by Fuhrmeister et al. (2011), their figs 1–3 showed a strong correlation between Hα and Ca II H&K (albeit at a lower observation cadence necessitated by the longer exposure times required in the blue arm of UVES with an M6V star). Since the infrared Ca II triplet lines are heavily blended, we have determined the variability in Ca II 8662 Å by subtracting the mean spectrum (derived from all observations). The relative EW was then measured for each observation. We find that the correlation between Hα and Ca II 8662 Å EW values is very strong, with Pearson correlation coefficients of $r = 0.92$, 0.94 and 0.91 for each of the three nights. The Ca II triplet lines are thus potentially useful for identifying strong flaring events, although the strength of Hα makes it the more useful line for activity monitoring in the first instance.

5.5.5 *Selection of RVs based on activity events*

A very large flare was observed during the observations of CN Leo (Reiners 2009) that lead to 660 m s^{-1} deviation from the other RVs that were measured with ∼10 m s^{-1} precision. For all other flare events resulting in $\log_{10}(L_{H\alpha}/L_{bol})$ changes of ≤0.4 dex, Reiners (2009) found no RV variability at the 10 m s^{-1} precision of the observations. The conclusion from that study is that only the very strongest flares, which are easily identifiable in spectra, affect RVs at the level of ∼500 m s^{-1}. The large flare on Proxima Centauri on 2009 March 14 resulted in a change of Hα emission of 0.33 dex (comparing the immediate pre-flare and maximum flare EWs). Our rms precision on 2009 March 14 was 5.84 m s^{-1} (full four-parameter correction). However, excursions of up to 20 m s^{-1} can occasionally be seen in the bottom panels of Fig. 2 that do not necessarily coincide with the flaring events presented in Fuhrmeister et al. (2011). Before and after the sudden rise in Hα emission corresponding to the large flare on 2009 March 14, the RVs appear to be relatively stable (Fig. 2, bottom-right panel) in the $t \sim 4.23$–4.25 d and 4.28–4.30 d regions. However, from $t \sim 4.26$–4.28 d, there is systematic RV deviation of ∼20 m s^{-1} coinciding with the onset and peak of the flare. It is difficult to determine whether the flare is responsible since systematic deviations of similar magnitude occur on 2009 March 12 and earlier on 2009 March 14. No strong flare counterpart is seen in the other activity indicators presented in Fuhrmeister et al. (2011) for these RV deviations. The correlation coefficient between Hα EWs and RVs for the complete Proxima Centauri data set is $r = -0.09$. For the region where Hα EW increases and the RVs show the tentative peak ($t = 4.255$–4.276 d), $r = -0.28$, indicating a weak negative correlation. The behaviour of Hα is more complex however during this strong flare cascade. Fig. 3 in Fuhrmeister et al. (2011) shows that the Hϵ and H I 3770 Å lines exhibit a more clearly defined peak (i.e. a sharper decline after the sharp rise at *XMM—Newton* wavelengths) that may indicate a higher correlation with the RVs. In conclusion, it is not clear that the strong flare really impacted on our RVs in this case and there is no evidence that any of the other flare events affected the RVs on Proxima Centauri at the 4–6 m s^{-1} level during the three nights of the observations.

Although the evidence suggests that moderate flaring does not affect RV measurements at ≥10 m s^{-1} on *slow* rotators, it is not clear whether this is also true for *moderate* rotators. In this instance, activity-related transients might be more clearly resolved owing to Doppler broadening of the lines. If we remove the observation

of LP 759-25 ($v \sin i = 13.7\,\mathrm{km\,s^{-1}}$), which shows H$\alpha$ in strong emission and evidence for a large flare (in both Hα and Ca II 8662 Å), the measured rms reduces from 79.9 $\mathrm{km\,s^{-1}}$ (line bisector corrected) to 29.7 $\mathrm{km\,s^{-1}}$. While this represents a dramatic improvement, and is now twice our predicted photon-noise-limited precision of 15 $\mathrm{m\,s^{-1}}$ (see earlier discussion in this section), it is difficult to determine the significance given that the rms values are based on only four and three observations alone, respectively.

It is thus clear that more observations are needed for each star because if late M stars are moderate rotators on average that show modulated activity, then measuring precise RVs at the sub-10 $\mathrm{m\,s^{-1}}$ level will prove extremely challenging. De-trending of RVs using activity indicators generally utilizes of the order of 20–30 epochs, at which stage planetary signals can be well characterized (e.g. see Bonfils et al. 2013). Monitoring of activity indicators for strong flaring events in late M dwarfs is also essential. For CN Leo (Reiners 2009), only ∼4 per cent of observations were affected by a strong flare. We also see very tentative evidence (with weak correlation), for RVs affected by flare activity (at the 20 $\mathrm{m\,s^{-1}}$ level) in ∼4 per cent of the Proxima Centauri observations.

6 CONCLUSION AND FUTURE PROSPECTS

With careful wavelength calibration we have demonstrated that 2.4 $\mathrm{m\,s^{-1}}$ precision can be achieved with UVES operating in the red part of the optical. Since we have so far only obtained three to five RV measurements per star spanning six nights, further observations are required before any potential planetary signals can be discerned. However, under the assumption that the current rms estimates are representative of a larger set of observations, and by considering our most stable targets that exhibit rms $< 16\,\mathrm{m\,s^{-1}}$, we can rule out the presence of planets with $m_\mathrm{p} \sin i > 10\,\mathrm{M}_\oplus$ in 0.03 au orbits. Extending this to include the less stable stars, our observations do not support evidence for planets more massive than $m_\mathrm{p} \sin i = 0.5\ M_\mathrm{J}$ at 0.03 au. Fig. 9 illustrates the late M parameter space of this investigation, presenting our ROPS targets, the early M dwarfs and all planets detected with RVs, orbiting stars up to 2 $\mathrm{M}_\odot$. The RVs corrected with the stellar line BIS are plotted as upper limits, and at present are only intended to illustrate the sensitivities achieved with our survey.

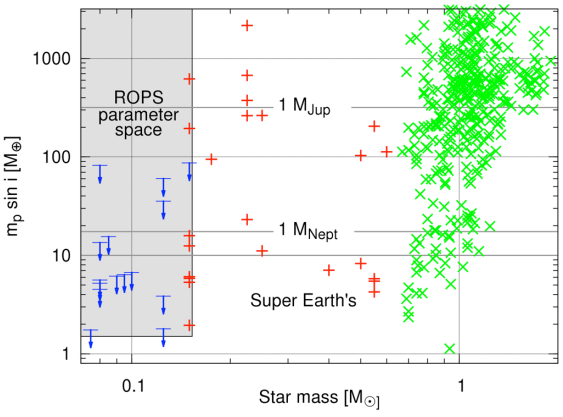

Figure 9. The unique parameter space explored by ROPS and current rms limits (blue filled circles with downward arrows indicating upper limits). Also shown are the M dwarfs with known planetary companions (red crosses) and all known planets with RV measurements (up to 2 solar masses) and hence $m_\mathrm{p} \sin i$ determinations.

Even a modest survey, targeting relatively small numbers of M dwarfs, leads us to expect significant numbers of low-mass planets, following the findings of recent studies (e.g. Bonfils et al. 2013; Dressing & Charbonneau 2013; Kopparapu 2013). It is vitally important however that if precisions of a few $\mathrm{m\,s^{-1}}$ are to be obtained in a large sample of stars, the activity must be clearly characterized and understood. This study was motivated by the uncharted late M dwarfs, hence our inclusion of target stars that were typical, in terms of activity and rotation. Even with the few observations presented here, it is clear that any future surveys must carefully select targets that do not bias the sample. In other words, selection of only slowly rotating late M dwarfs might lead to observation of predominantly low axial inclination systems ($i \ll 90^\circ$) that are not as favourable for RV planet detection. For instance, if the mean axial inclination of a stellar population is assumed to be 45°, and if the mean $v \sin i$ is found to be 8 $\mathrm{km\,s^{-1}}$ for a typical M6V (Jenkins et al. 2009), selection of stars with $v \sin i < 5\,\mathrm{km\,s^{-1}}$ will lead to a sample biased to a mean axial inclination of $i < 26^\circ$. The problem becomes worse for an M9V star with a typical $v \sin i = 15\,\mathrm{km\,s^{-1}}$. Here we expect that observation of stars with $v \sin i < 5\,\mathrm{km\,s^{-1}}$ will lead to a sample with a mean axial inclination of $i < 14^\circ$ (i.e. very close to pole-on). Conversely, we find that significant $v \sin i$ leads to higher rms, and most importantly that these rms values are significantly above the photon-noise-limited precision at the observed $v \sin i$ and S/N ratios. Hα luminosity, $\log_{10}(L_\mathrm{H\alpha}/L_\mathrm{bol})$, shows a clear trend with rms as discussed in Section 5.5.3 and illustrated in Fig. 8. The implication that late-type stars are significantly spotted, and hence exhibit time-varying line distortions, suggests that ways of mitigating the effects of the resulting 'jitter' are important for this class of stars.

In this paper, we used a standard and straightforward bisector span analysis to de-trend the data. Only further observations will enable this procedure to be fully validated. At the same time, a simple BIS analysis is not able to properly remove any magnetically induced RV signatures to the photon-noise level, especially for stars with moderate rotation. We will investigate this in a future publication, but our preliminary simulations indicate that the BIS analysis is optimal for a narrow range of rotation velocities. Any starspot distributions are also an important consideration. In Barnes, Jeffers & Jones (2011) for example, we assumed the effects of randomly distributed spots, but did not try to remove their influence on the RV jitter. It is not at all clear that random spots, resulting from a fully convective turbulent dynamo, are the predominant spot pattern on active late M spectral types. By mid-M when stars become fully convective, there is evidence that magnetic fields become dipolar (Donati et al. 2008; Morin et al. 2008). Doppler images are one means of characterizing spot patterns, but photospheric brightness images have currently only been derived for early M stars (Barnes & Collier Cameron 2001; Barnes, James & Cameron 2004; Phan-Bao et al. 2009).

Observing strategies are also an important consideration when trying to mitigate any starspot effects. Moulds et al. (2013) have found that starspot jitter can largely be removed by modelling starspot effects on the line profile. Hence, intensive spectroscopic observations of late M targets may be necessary to enable more effective removal of activity signatures. Fortuitously, M6V–M9V planets are expected in a close orbit about their parent stars (Bonfils et al. 2013), which as already noted lead us to expect 6–11 d orbits at the centre of the continuous HZ (Kopparapu et al. 2013). Hence, observations over week–month-long time-scales over which starspot groups are stable (Goulding et al. 2012) should enable good sampling of M dwarf planet orbits while simultaneously providing the observations that could help remove activity jitter. In addition,

the use of Bayesian techniques to search for low-amplitude signals in noise enables recovery of RV signatures in only a few epochs. Indeed, we find low-amplitude signals in the HARPS early-mid M dwarf sample (Tuomi et al. 2014) that indicate that RV signals are abundant, with occurrence rates of $0.06^{+0.11}_{-0.03}$ for $3 \leq m_{\rm p} \sin i \leq 10\,{\rm M}_{\oplus}$ in 1–10 d orbits, increasing to $1.02^{+1.48}_{-0.69}$ for 10–100 d planets (i.e. an upper limit of greater than one planet per star). Moreover, the estimated HZ occurrence rate for $3 \leq m_{\rm p} \sin i \leq 10\,{\rm M}_{\oplus}$ is found to be $\eta_{\oplus} = 0.16$–0.24. By extrapolation from early M dwarf observations, we expect late M dwarf planet frequencies to peak in shorter orbits, continuing the trend of semi-major axis distribution versus stellar mass noted by Currie (2009). For example, the 33 d, 0.135 au orbit (Kopparapu et al. 2013) of an HZ planet hosted by $0.3\,{\rm M}_{\odot}$ early M dwarf would reduce to an 11 d, 0.045 au orbit for the sample planet hosted by a $0.1\,{\rm M}_{\odot}$ star. Further to the above argument, this illustrates that short observing campaigns should quickly uncover significant signals for surveys that enable few $\rm m\,s^{-1}$ precision to be attained. The search for low-mass planets orbiting the lowest mass stars is thus a challenging but achievable goal with current estimates leading us to expect a host of interesting planets in the near future.

ACKNOWLEDGEMENTS

We would like to thank the anonymous referee for the suggested amendments and for careful reading of the manuscript. JB gratefully acknowledges funding through a University of Hertfordshire Research Fellowship. JSJ acknowledges funding by Fondecyt through grant 3110004 and partial support from Centro de Astrofísica FONDAP 15010003, the GEMINI-CONICYT FUND and from the Comité Mixto ESO-GOBIERNO DE CHILE. SVJ acknowledges research funding by the Deutsche Forschungsgemeinschaft (DFG) under grant SFB 963/1, project A16. DM and PA gratefully acknowledge support by the FONDAP Center for Astrophysics 15010003, the BASAL CATA Center for Astrophysics and Associated Technologies PFB-06 and the MILENIO Milky Way Millennium Nucleus from the Ministry of Economys ICM grant P07-021-F. AJ acknowledges support from FONDECYT project 1130857, BASAL CATA PFB-06 and the Millennium Science Initiative, Chilean Ministry of Economy (Millennium Institute of Astrophysics MAS and Nucleus P10-022-F). PR also acknowledges FONDECYT project 1120299. During the course of this work, DJP and MT were supported by RoPACS, a Marie Curie Initial Training Network funded by the European Commissions Seventh Framework Programme. JB, JSJ, DJP and SVJ have also received travel support from RoPACS during this research. This paper includes data gathered with the 6.5 m Magellan Telescopes located at Las Campanas Observatory, Chile.

REFERENCES

Allard F., Hauschildt P. H., Alexander D. R., Tamanai A., Schweitzer A., 2001, ApJ, 556, 357
Anglada-Escudé G., Butler R. P., 2012, ApJ, 200, 15
Bailey J. I. III, White R. J., Blake C. H., Charbonneau D., Barman T. S., Tanner A. M., Torres G., 2012, ApJ, 749, 16
Baliunas S. et al., 1995, ApJ, 438, 269
Barber R. J., Tennyson J., Harris G. J., Tolchenov R. N., 2006, MNRAS, 368, 1087
Barnes J. R., Collier Cameron A., 2001, MNRAS, 326, 950
Barnes J. R., Collier Cameron A., James D. J., Steeghs D., 2001, MNRAS, 326, 1057
Barnes J. R., James D. J., Cameron A. C., 2004, MNRAS, 352, 589
Barnes J. R., Barman T. S., Prato L., Segransan D., Jones H. R. A., Leigh C. J., Collier Cameron A., Pinfield D. J., 2007, MNRAS, 382, 473
Barnes J. R., Jeffers S. V., Jones H. R. A., 2011, MNRAS, 412, 1599
Barnes J. R. et al., 2012, MNRAS, 424, 591 (B12)
Barnes J. R. et al., 2013, in Saglia R., ed., European Physical Journal Web of Conferences, Vol. 47, Hot Planets and Cool Stars. EDP Sciences, Les Ulis, p. 5002
Bean J. L., Seifahrt A., Hartman H., Nilsson H., Wiedemann G., Reiners A., Dreizler S., Henry T. J., 2010, ApJ, 713, 410
Bell K. J., Hilton E. J., Davenport J. R. A., Hilton E. J., Davenport J. R. A., Hawley S. L., West A. A., Rogel A. B., 2012, PASP, 124, 14
Bonfils X. et al., 2013, A&A, 549, A109
Borucki W. J. et al., 2011, ApJ, 736, 19
Brott I., Hauschildt P. H., 2005, in Turon C., O'Flaherty K. S., Perryman M. A. C., eds, ESA Special Publication, Vol. 576, The Three-Dimensional Universe with Gaia. ESA, Noordwijk, p. 565
Butler R. P., Marcy G. W., Williams E., McCarthy C., Dosanjh P., Vogt S. S., 1996, PASP, 108, 500
Clough S. A., Iacono M. J., Moncet J. L., 1992, J. Geophys. Res., 97, 15761
Clough S. A., Shephard M. W., Mlawer E. J., Delamere J. S., Iacono M. J., Cady-Pereira K., Boukabara S., Brown P. D., 2005, J. Quant. Spectrosc. Radiat. Transfer, 91, 233
Currie T., 2009, ApJ, 694, L171
Delfosse X., Forveille T., Mayor M., Perrier C., Naef D., Queloz D., 1998, A&A, 338, L67
Donati J. et al., 2008, MNRAS, 390, 545
Dressing C. D., Charbonneau D., 2013, ApJ, 767, 95
Endl M., Kürster M., 2008, A&A, 488, 1149
Fabrycky D. C. et al., 2012, ApJ, 750, 114
Figueira P., Pepe F., Lovis C., Mayor M., 2010, A&A, 515, A106
Fuhrmeister B., Liefke C., Schmitt J. H. M. M., 2007, A&A, 468, 221
Fuhrmeister B., Lalitha S., Poppenhaeger K., Rudolf N., Liefke C., Reiners A., Schmitt J. H. M. M., Ness J.-U., 2011, A&A, 534, A133
Gerstenkorn S., Luc P., 1978, Atlas DU spectre d'absorption de la molecule d'iode 14800-20000 cm-1 (Paris: Editions du Centre National de la Recherche Scientifique (CNRS), 1978)
Goulding N. T. et al., 2012, MNRAS, 427, 3358
Gray D. F., 1983, in Stenflo J. O., ed., Proc. IAU Symp. 102, Solar and Stellar Magnetic Fields: Origins and Coronal Effects. Reidel, Dordrecht, p. 461
Gray D. F., Brown K. I. T., 2006, PASP, 118, 399
Griffin R., Griffin R., 1973, MNRAS, 162, 243
Heavens A. F., 1993, MNRAS, 263, 735
Horne K. D., 1986, PASP, 98, 609
Ida S., Lin D. N. C., 2005, ApJ, 626, 1045
Isaacson H., Fischer D., 2010, ApJ, 725, 875
Jenkins J. S., Ramsey L. W., Jones H. R. A., Pavlenko Y., Gallardo J., Barnes J. R., Pinfield D. J., 2009, ApJ, 704, 975
Jones H. R. A. et al., 2008, in McLean I. S., ed., Proc. SPIE, 7014, Ground-based and Airborne Instrumentation for Astronomy II. SPIE, Bellingham, p. 31
Kopparapu R. K., 2013, ApJ, 767, L8
Kopparapu R. K. et al., 2013, ApJ, 765, 131
Kürster M., Hatzes A. P., Cochran W. D., Döbereiner S., Dennerl K., Endl M., 1999, A&A, 344, L5
Latham D. W., Stefanik R. P., Mazeh T., Mayor M., Burki G., 1989, Nature, 339, 38
Lovis C., Pepe F., 2007, A&A, 468, 1115
Mahadevan S., Ge J., 2009, ApJ, 692, 1590
Mahadevan S. et al., 2012, Proc. SPIE, 8446, Ground-based and Airborne Instrumentation for Astronomy IV. Available at: http://dx.doi.org/10.1117/12.926102
Marcy G. W., Butler R. P., 1992, PASP, 104, 270
Marcy G. W., Butler R. P., Vogt S. S., Fischer D., Lissauer J. J., 1998, ApJ, 505, L147
Marsh T. R., Horne K., 1988, MNRAS, 235, 269
Martínez Fiorenzano A. F., Gratton R. G., Desidera S., Cosentino R., Endl M., 2005, A&A, 442, 775

Mohanty S., Basri G., 2003, ApJ, 583, 451
Morin J. et al., 2008, MNRAS, 390, 567
Moulds V. E., Watson C. A., Bonfils X., Littlefair S. P., Simpson E. K., 2013, MNRAS, 430, 1709
Muirhead P. S., Hamren K., Schlawin E., Rojas-Ayala B., Covey K. R., Lloyd J. P., 2012, ApJ, 750, L37
Pepe F. et al., 2011, A&A, 534, 58
Phan-Bao N., Lim J., Donati J.-F., Johns-Krull C. M., Martín E. L., 2009, ApJ, 704, 1721
Press W. H., Flannery B. P., Teukolsky S. A., Vetterling W. T., 1986, Numerical Recipes: The Art of Scientific Computing. Cambridge Univ. Press, Cambridge
Quirrenbach A. et al., 2012, Proc. SPIE 8446, Ground-based and Airborne Instrumentation for Astronomy IV. Available at: http://dx.doi.org/10.1117/12.925164
Redman S. L., Lawler J. E., Nave G., Ramsey L. W., Mahadevan S., 2011, ApJS, 195, 24
Reiners A., 2009, A&A, 498, 853
Reiners A., Basri G., 2009, ApJ, 705, 1416
Reiners A., Basri G., 2010, ApJ, 710, 924
Rodler F., Deshpande R., Zapatero Osorio M. R., Martín E. L., Montgomery M. M., Del Burgo C., Creevey O. L., 2012, A&A, 538, A141
Rothman L. S. et al., 2009, J. Quant. Spectrosc. Radiat. Transfer, 110, 533
Schrijver C. J., Cote J., Zwaan C., Saar S. H., 1989, ApJ, 337, 964
Shortridge K., 1993, in Hanisch R. J., Brissenden R. J. V., Barnes J., eds, ASP Conf. Ser. Vol. 52, Astronomical Data Analysis Software and Systems II. Astron. Soc. Pac., San Francisco, p. 219
Steffen J. H. et al., 2013, MNRAS, 428, 1077
Toner C. G., Gray D. F., 1988, ApJ, 334, 1008
Tonry J., Davis M., 1979, AJ, 84, 1511
Tuomi M., Jones H. R. A., Barnes J. R., Jenkins J. S., Anglada-Escudé G., 2014, MNRAS, submitted
West A. A., Hawley S. L., 2008, PASP, 120, 1161
West A. A. et al., 2004, AJ, 128, 426
Wilson O. C., 1978, ApJ, 225, 396
Wright J. T., Marcy G. W., Butler R. P., Vogt S. S., 2004, ApJS, 152, 261
Ycas G. G. et al., 2012, Opt. Express, 20, 6631
Zechmeister M., Kürster M., Endl M., 2009, A&A, 505, 859

APPENDIX A: RADIAL VELOCITIES

The RV measurements are calculated via the procedures described in this paper, using line lists derived from GJ 1061 (M5.5V) and LHS 132 (M8V). Two observations were made of GJ 1061 at high resolution (0.4 arcsec slit) and were co-aligned, co-added and normalized to a value of 1.0 to obtain a template for empirical determination of the line list. Similarly, all four observations of LHS 132 were aligned to the first observation (0.8 arcsec slit) and the resulting template normalized to a value of 1.0. The line lists were derived by identifying the minima of absorption features in the templates and fitting quadratics to the three lowest values in each absorption line. The line depth and wavelength of each line were thus recorded.

Since we did not observe an RV standard, all RVs are determined relative to the template used for deconvolution. The mean heliocentrically corrected velocity of the RV observations of each of the template stars is first determined. For GJ 1061, we find $\Gamma_{\rm GJ\,1061} = 14\,499.07\,{\rm m\,s^{-1}}$ and for LHS 132, $\Gamma_{\rm LHS\,132} = 18\,661.17\,{\rm m\,s^{-1}}$. In other words, the RVs listed for GJ 1061 (Tables A1 and A2) and LHS 132 (Table A3) have been determined by subtracting the indicated $\Gamma_{\rm GJ\,1061}$ and $\Gamma_{\rm LHS\,132}$ values. The velocities relative to the reference frame of GJ 1061 can thus be obtained from columns 2, 4, 5 and 6 of Table A1 and columns 2, 4 and 5 of Table A2. Similarly, the velocities relative to the reference

Table A1. Observation times and velocities for Proxima Centauri. The $\Gamma_{\rm ProxCen}$ velocity must be added to the individual velocities to transform them into the reference frame of GJ 1061 (from which the deconvolution template was derived). Columns 1–3 give the Julian date, the velocities before atmospheric correction relative to $\Gamma_{\rm ProxCen}$ (as presented in the upper panels of Fig. 2) and the propagated uncertainty for each observation. The velocities after the atmospheric correction is applied to each night individually are given in column 4 (I corr) and for all nights together in column 5 (A corr). See Section 4.3 for details.

JD	RV ($\rm m\,s^{-1}$) No corr	RV error ($\rm m\,s^{-1}$)	RV ($\rm m\,s^{-1}$) I corr	RV ($\rm m\,s^{-1}$) A corr
Proxima Centauri ($\Gamma_{\rm ProxCen} = -22\,344.98\,{\rm m\,s^{-1}}$)				
245 4900.134 561	44.24	7.08	0.00	0.00
245 4900.136 059	36.43	6.02	3.69	−5.47
245 4900.137 557	41.09	6.07	−3.85	−12.82
245 4900.139 055	36.46	6.84	1.05	−7.72
245 4900.140 552	43.11	6.56	−3.33	−11.90
245 4900.142 048	35.45	6.73	3.58	−4.80
245 4900.143 546	34.04	5.99	−3.85	−12.02
245 4900.145 049	41.68	7.29	−5.03	−13.00
245 4900.146 545	35.18	5.79	2.84	−4.93
245 4900.148 045	36.54	6.37	−3.44	−11.01
245 4900.149 547	43.95	6.55	−1.86	−9.23
245 4900.151 045	49.28	7.01	5.77	−1.40
245 4900.152 543	33.51	6.28	11.30	4.33
245 4900.154 043	36.71	6.40	−4.26	−11.03
245 4900.155 546	35.31	6.49	−0.86	−7.42
245 4900.157 045	38.47	5.80	−2.09	−8.44
245 4900.158 541	37.84	5.89	1.26	−4.89
245 4900.160 038	48.72	6.73	0.83	−5.12
245 4900.161 536	38.19	6.22	11.87	6.13
245 4900.163 032	41.80	6.52	1.53	−4.02
245 4900.164 534	35.23	6.28	5.31	−0.03
245 4900.166 037	42.76	6.41	−1.10	−6.24
245 4900.167 537	40.66	6.51	6.60	1.66
245 4900.169 039	28.53	6.35	4.66	−0.07
245 4900.170 536	37.53	7.09	−7.31	−11.85
245 4900.172 035	31.18	6.29	1.85	−2.49
245 4900.173 536	35.62	7.02	−4.37	−8.50
245 4900.175 038	36.42	6.43	0.24	−3.70
245 4900.176 538	29.02	5.84	1.17	−2.56
245 4900.178 037	35.78	6.73	−6.09	−9.62
245 4900.179 535	29.29	5.49	0.81	−2.54
245 4900.181 036	32.33	5.09	−5.56	−8.70
245 4900.182 533	33.84	5.82	−2.38	−5.33
245 4900.184 029	29.40	6.15	−0.74	−3.50
245 4900.185 530	33.65	6.10	−5.04	−7.62
245 4900.187 028	34.94	6.04	−0.67	−3.05
245 4900.188 531	29.71	6.75	0.74	−1.45
245 4900.190 033	29.76	5.55	−4.36	−6.37
245 4900.191 532	28.58	5.23	−4.19	−6.02
245 4900.193 034	29.90	5.23	−5.26	−6.90
245 4900.194 535	34.38	6.42	−3.82	−5.27
245 4900.196 035	27.25	4.95	0.77	−0.51
245 4900.197 537	36.39	4.82	−6.25	−7.35
245 4900.199 039	33.26	3.40	2.99	2.07
245 4900.200 540	35.44	3.70	−0.02	−0.76
245 4900.202 039	26.18	4.51	2.25	1.69
245 4900.203 541	32.65	5.06	−6.89	−7.29
245 4900.205 041	32.21	5.50	−0.31	−0.54

Table A2. Observation times and radial velocities for all M5V–M7V ROPS targets deconvolved with the GJ 1061 line list. The Γ_* velocity indicated in each case must be added to the velocities to transform them into the reference frame of GJ 1061 (from which the deconvolution template was derived). Columns 1–6 give Julian date, raw radial velocity with Γ_* subtracted (No corr), propagated error, stellar line bisector-corrected velocity (L corr), telluric bisector-corrected velocity (T corr) and stellar line minus telluric line bisector-corrected velocity (L-T corr).

JD	RV ($m\,s^{-1}$) No corr	RV error ($m\,s^{-1}$)	RV ($m\,s^{-1}$) L corr	RV ($m\,s^{-1}$) T corr	RV ($m\,s^{-1}$) L-T corr
		GJ 3076 ($\Gamma_{GJ\,3076} = 2449.11\,m\,s^{-1}$)			
245 6131.834 179	−9.18	11.55	−49.64	−41.32	39.43
245 6132.832 890	137.39	23.09	116.00	52.32	1.98
245 6134.859 510	−23.93	18.38	27.71	62.41	21.24
245 6137.817 710	−104.28	35.85	−94.08	−73.41	−62.65
		GJ 1002 ($\Gamma_{GJ\,1002} = -40\,733.57\,m\,s^{-1}$)			
245 6131.766 112	11.95	6.32	−1.05	−12.68	20.81
245 6132.763 310	−38.07	4.04	−4.50	−2.18	−33.53
245 6134.782 990	−4.52	5.44	7.19	−2.81	7.76
245 6137.825 820	30.64	9.62	−1.65	17.67	4.96
		GJ 1061 ($\Gamma_{GJ\,1061} = 14\,499.07\,m\,s^{-1}$)			
245 6131.905 029	5.54	11.48	2.98	3.61	2.39
245 6132.912 720	0.58	5.16	2.08	1.01	3.62
245 6132.917 280	−1.58	4.87	−1.92	−1.98	−1.74
245 6134.920 640	1.47	7.44	−2.25	−2.21	−1.64
245 6137.897 020	−6.01	6.80	−0.89	−0.43	−2.63
		LP 759-25 ($\Gamma_{LP\,759\text{-}25} = 15\,661.08\,m\,s^{-1}$)			
245 6131.751 882	−81.56	18.58	18.70	−72.16	21.35
245 6132.750 070	−75.07	9.53	−76.08	34.48	−40.98
245 6134.768 600	147.79	14.79	104.11	81.46	83.02
245 6137.709 730	8.83	14.24	−46.73	−43.78	−63.39
		GJ 3146 ($\Gamma_{GJ\,3146} = 14\,908.17\,m\,s^{-1}$)			
245 6131.894 923	−64.05	14.20	−44.64	−40.08	−9.85
245 6132.904 030	59.38	8.88	66.48	8.83	−2.06
245 6134.937 430	−84.83	20.23	−10.32	−76.91	7.99
245 6137.887 810	89.51	26.83	−11.52	108.15	3.91
		GJ 3128 ($\Gamma_{GJ\,3128} = 20\,020.94\,m\,s^{-1}$)			
245 6131.842 671	33.86	13.54	2.29	35.22	7.38
245 6132.840 830	−15.79	6.95	0.29	−15.09	−3.64
245 6134.869 770	1.77	7.54	12.66	−4.27	16.28
245 6137.835 510	−19.85	7.97	−15.23	−15.86	−20.02
		GJ 4281 ($\Gamma_{GJ\,4281} = -7408.90\,m\,s^{-1}$)			
245 6131.735 050	40.61	10.94	14.92	0.24	−4.93
245 6132.734 400	9.37	4.86	−13.31	2.08	21.38
245 6134.741 200	−2.04	5.68	−3.18	−2.78	−2.13
245 6137.694 200	−47.94	12.84	1.57	0.47	−14.32
		SO J025300.5+165258 ($\Gamma_{SO\,J0253+1652} = 64\,010.47\,m\,s^{-1}$)			
245 6131.912 948	2.39	13.48	−6.51	3.37	−3.83
245 6132.925 100	−20.07	4.53	−14.29	−18.20	−17.08
245 6134.929 120	16.80	9.96	10.94	4.94	17.97
245 6137.905 420	0.87	10.56	9.86	9.89	2.94

frame of LHS 132 can be obtained from columns 2, 4 and 5 of Table A3.

For all other targets, we indicate the deconvolution template used (either GJ 1061 or LHS 132) and the value Γ_* (where * denotes the star) that must be added to the tabulated velocities in order to place them in the reference frame of that template. We tabulate the Γ_* subtracted values (i.e. zero mean) for consistency with Fig. 5 which makes the RV variability easier to discern.

Table A3. Observation times and velocities for the M7.5V–M9V targets deconvolved with the LHS 132 line list.

JD	RV ($m\,s^{-1}$) No corr	RV error ($m\,s^{-1}$)	RV ($m\,s^{-1}$) L corr	RV ($m\,s^{-1}$) T corr	RV ($m\,s^{-1}$) L-T corr
LP 888-18 ($\Gamma_{\rm LP\,888\text{-}18} = 25\,171.22\,m\,s^{-1}$)					
245 6131.858 119	−61.82	26.26	−51.26	−30.83	−38.66
245 6132.864 200	21.77	6.11	13.88	−21.16	−13.01
245 6134.885 720	43.01	9.99	8.22	37.02	51.60
245 6137.851 140	−2.97	11.35	29.16	14.97	0.07
LHS 132 ($\Gamma_{\rm LHS\,132} = 18\,661.17\,m\,s^{-1}$)					
245 6131.803 782	0.03	15.84	1.97	−3.04	−5.82
245 6132.799 410	13.05	6.64	15.07	10.81	13.53
245 6134.824 210	−4.33	8.73	−2.32	−7.33	−4.63
245 6137.784 340	−16.72	13.51	−14.72	−0.44	−3.08
2MASS J23062928−0502285 ($\Gamma_{\rm 2M\,J23\text{-}05} = -51\,688.03\,m\,s^{-1}$)					
245 6131.716 866	−40.55	15.19	−14.89	−6.83	0.17
245 6132.714 250	−1.12	6.58	12.99	−19.35	−13.81
245 6134.721 330	19.56	9.64	11.21	6.09	3.93
245 6137.728 420	22.11	19.30	−9.31	20.09	9.71
LHS 1367 ($\Gamma_{\rm LHS\,1367} = 657.43\,m\,s^{-1}$)					
245 6131.821 169	−5.43	8.95	−17.23	−7.49	−2.41
245 6132.818 410	22.57	4.65	7.97	0.87	18.50
245 6134.844 390	12.19	6.02	16.77	22.06	14.71
245 6137.803 370	−29.32	7.56	−7.51	−15.43	−30.80
LP 412-31 ($\Gamma_{\rm LP412\text{-}31} = 46\,612.38\,m\,s^{-1}$)					
245 6131.925 114	152.74	12.83	13.71	192.41	−69.72
245 6132.934 000	139.53	10.68	215.47	88.73	138.13
245 6137.917 920	−292.27	17.15	−229.18	−281.14	−68.42
2MASS J23312174−2749500 ($\Gamma_{\rm 2M\,J23\text{-}27} = 261.26\,m\,s^{-1}$)					
245 6131.782 437	−53.61	11.25	−54.65	−27.25	−20.69
245 6132.779 070	21.80	6.06	21.11	30.22	30.79
245 6134.801 980	3.71	7.50	11.93	−23.18	0.40
245 6137.761 310	28.10	11.44	21.62	20.20	−10.50
2MASS J03341218−4953322 ($\Gamma_{\rm 2M\,J03\text{-}49} = 73\,732.21\,m\,s^{-1}$)					
245 6131.879 267	−2.05	7.31	−1.64	−8.18	−9.37
245 6132.886 170	−14.65	5.18	−5.81	−2.95	−4.68
245 6134.906 790	5.63	7.63	9.08	7.29	6.13
245 6137.872 580	11.07	8.16	−1.63	3.84	7.92

Table A4. Radial velocities for GJ 1061 and GJ 1002 derived using TERRA (see Section 5.4). The spectra were taken from the ESO HARPS archive.

JD	RV ($m\,s^{-1}$)	RV error ($m\,s^{-1}$)
GJ 1061		
245 2985.713 012	0.35	1.09
245 2996.737 269	0.00	1.23
245 3337.748 816	−3.51	0.85
245 4341.868 575	−3.18	0.93
GJ 1002		
245 3336.603 252	3.01	1.66
245 3918.940 758	0.00	1.69
245 4048.614 913	−0.61	1.64
245 4800.563 001	−2.58	1.42

SUPPORTING INFORMATION

Additional Supporting Information may be found in the online version of this article:

Table A1. Observation times and velocities for Proxima Centauri (http://mnras.oxfordjournals.org/ lookup/suppl/doi:10.1093/mnras/stu172/-/DC1).

Please note: Oxford University Press is not responsible for the content or functionality of any supporting materials supplied by the authors. Any queries (other than missing material) should be directed to the corresponding author for the article.

This paper has been typeset from a TEX/LATEX file prepared by the author.